Nano-scale Architecture of Blood-Brain Barrier Tight-Junctions

Esther Sasson[1], Shira Anzi[1], Batia Bell[1], Oren Yakovian[2], Meshi Zorsky[3], Urban Deutsch[4], Britta Engelhardt[4], Eilon Sherman[2], Gad D. Vatine[3], Ron Dzikowski[5], Ayal Ben-Zvi[1*].

1. Department of Developmental Biology and Cancer Research, The Institute for Medical Research Israel-Canada, Faculty of Medicine, Hebrew University of Jerusalem, Jerusalem 91120, Israel

2. Racah Institute of Physics, The Hebrew University, Jerusalem 9190401, Israel

3. The Department of Physiology and Cell Biology, Faculty of Health Sciences, The Regenerative Medicine and Stem Cell (RMSC) research Center and the Zlotowski Center for Neuroscience, Ben-Gurion University of the Negev, Beer Sheva 84105, Israel

4. Theodor Kocher Institute, University of Bern, Bern, Switzerland.

5. Department of Microbiology and Molecular Genetics, The Kuvin Center for the Study of Infectious and Tropical Diseases, IMRIC, Faculty of Medicine, Hebrew University of Jerusalem, Jerusalem 91120, Israel.

*** Address correspondence to:**

Ayal Ben-Zvi, PhD

Department of Developmental Biology and Cancer Research,

The Institute for Medical Research Israel-Canada,

Faculty of Medicine,

Hebrew University of Jerusalem,

Jerusalem 91120, Israel

Tel: +972-2-6787624

Email: Ayalb@ekmd.huji.ac.il

Abstract

Tight junctions (TJs) between blood-brain barrier (BBB) endothelial cells construct a robust physical barrier, whose damage underlies BBB dysfunctions related to several neurodegenerative diseases. What makes these highly specialized BBB-TJs extremely restrictive remains unknown. Here, we use super-resolution microscopy (dSTORM) to uncover new structural and functional properties of BBB TJs. Focusing on three major components, Nano-scale resolution revealed sparse (occludin) vs. clustered (ZO1/claudin-5) molecular architecture. Developmentally, permeable TJs become first restrictive to large molecules, and only later to small molecules, with claudin-5 proteins arrangement compacting during this maturation process. Mechanistically, we reveal that ZO1 clustering is independent of claudin-5 *in-vivo*. In contrast to accepted knowledge, we found that in the developmental context, total levels of claudin-5 inversely correlate with TJ functionality. Our super-resolution studies provide a unique perspective of BBB TJs and open new directions for understanding TJ functionality in biological barriers, ultimately enabling restoration in disease or modulation for drug delivery.

Introduction

The blood-brain barrier (BBB) was identified when dye/tracer injected into the blood circulation reached the majority of body tissues but failed to penetrate the brain (Hagan & Ben-Zvi, 2015). Endothelial cells (ECs) were identified as the core component of the mammalian BBB when electron microscopy (EM) allowed imaging of fine ultra-structural cell-biology components of BBB cells (Brightman & Reese, 1969; Reese & Karnovsky, 1967). Horseradish-peroxidase (HRP) used as an EM compatible tracer revealed that BBB ECs lack fenestrations (openings traversing the entire cell width) and exhibit extremely low

rates of transcytosis (vesicular transport), both mediating intracellular permeability in peripheral ECs. A central discovery of these studies was that tight junctions (TJs) between neighboring ECs are responsible for intercellular restrictive barrier properties (Brightman & Reese, 1969; Reese & Karnovsky, 1967). Ever since, BBB TJs became a major focus of the BBB research field; TJs modulation is explored as means to enhance brain drug delivery, and TJs damage is investigated to better understand underlying BBB dysfunctions implicated in diseases (neurodegenerative, neuro-inflammatory, trauma etc. (Bauer, Krizbai, Bauer, & Traweger, 2014; Greene et al., 2018; Hagan & Ben-Zvi, 2015; Kealy, Greene, & Campbell, 2018; Knowland et al., 2014; Liebner et al., 2018; Sweeney, Sagare, & Zlokovic, 2018; Zhao, Nelson, Betsholtz, & Zlokovic, 2015; Zlokovic, 2008)).

Several gene families encoding integral membrane proteins (e.g occludin, junctional adhesion molecules (JAMs), claudins, and tricellulins (LSR/Marveld)) and adaptors that link TJs to the cytoskeleton (such as zonula occludens (ZO)), participate in constructing BBB TJs (Bauer et al., 2014; Furuse, Fujita, Hiiragi, Fujimoto, & Tsukita, 1998; Furuse et al., 1993; Haseloff, Dithmer, Winkler, Wolburg, & Blasig, 2015; Knowland et al., 2014; Langen, Ayloo, & Gu, 2019; Martin-Padura et al., 1998; Morita, Sasaki, Furuse, & Tsukita, 1999; Nitta et al., 2003; Sohet et al., 2015). Immunofluorescence and imaging with conventional light microscopy provided insights into the molecular components of TJs. Nevertheless, these approaches do not enable proper resolution for nano-scale imaging of TJ architecture. Electron microscopy on the other hand, provides superb resolution to image cellular structures but is much less effective in simultaneously localizing multiple proteins and tracer molecules, limiting our ability to study the molecular architecture of TJs. In order to bridge the gap between these two imaging methodologies and overcome their limitations, we developed an approach to image the BBB with direct stochastic optical reconstruction microscopy (dSTORM (van de Linde et al., 2011)) and study TJs at the nano-scale level.

Results

Super-resolution microscopy of endothelial tight junctions

We hypothesized that effective imaging of multiple TJ proteins organized in a very tight spatial localization could be achieved with dSTORM. To evaluate this approach we used bEND.3 cells (a mouse brain-derived endothelioma cell-line), cultured *in vitro* to form a confluent monolayer. These cells were shown to form TJs in a gradual process that includes translocation of claudin-5 from cytoplasmic and general membrane localizations to the cell boundaries in contact between adjacent cells (Koto et al., 2007). We confirmed these observations with immunofluorescence labeling claudin-5 and ZO1 in several time points after the cultures reached confluence state (Fig. 1a). Previous studies also demonstrated that during this process, claudin-5 expression is increased reaching maximal levels by three days post-confluence. The monolayer trans-endothelial electrical resistance (TEER), a proxy for TJ function reflecting intercellular restrictive properties, is elevated reaching maximal levels by seven days post-confluence (Koto et al., 2007).

We therefore further investigated two states: post-confluence (3-7 days post-confluence) and super-confluence (more than 11 days post-confluence). Using antibodies against claudin-5 and ZO1 for immunofluorescence and dSTORM imaging, we demonstrated a new layer of complexity in TJ organization (Fig. 1b-e). Most TJ studies use the term ‘strands’ to describe the organization of TJ proteins in a continuous line around the boundaries of the cells (as seen in Fig. 1a). Super resolution imaging allowed us to demonstrate that both claudin-5 (green) and ZO1 (red) are not organized in continuous lines but rather in disrupted lines with discrete clusters, forming bead-like structures (Fig. 1b). A pronounced change was found in the organization of the two TJ proteins at the cell-cell contacts: at post-confluence, signals along the membrane were more diffused, forming elongated clusters and ZO1 signals intermingled with claudin-5 signals (Fig. 1b, arrows). In contrast, at super-confluence, claudin-5 signals

106 along the membrane became concentrated in more discrete and shorter foci, flanking ZO1
107 signals (Fig. 1b, arrowheads).

108 Target proteins labeled with antibodies imaged with dSTORM produced resolved signals
109 representing an amplification of actual target numbers (see methods for details). Resolution of
110 approximately 20 nm allowed us to separate signals and to use these as proxies for the
111 abundance of target molecules, which could be used to compare different states. To quantify
112 the differences in TJ architecture during this *in vitro* process, we analyzed the images using a
113 custom clustering Matlab code to measure cluster area and number of signals per cluster.
114 These were used to calculate the signal densities for each cluster (see clustering simulation
115 Fig. 1c and methods for details). We could detect a clear shift towards smaller clusters with
116 more claudin-5 signals per cluster at super-confluence (Fig. 1d). Clusters with higher numbers
117 of signals were more abundant at this late state, especially in clusters with area smaller than
118 0.3 μm^2. Average signal density (per cluster) was also higher at the super-confluence state
119 (~4-fold, Fig. 1e, $P<0.0001$).
120

Figure 1

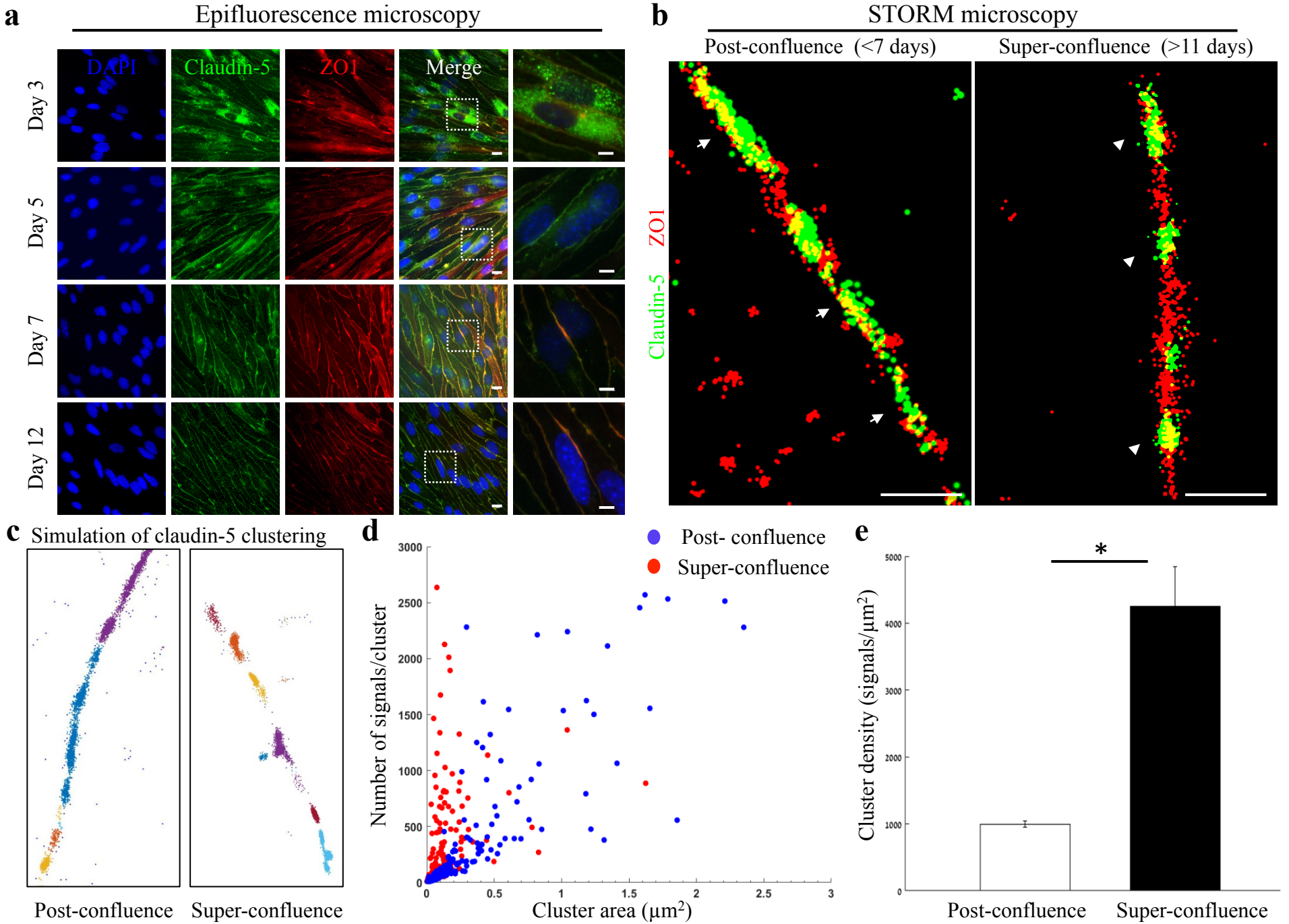
a
Epifluorescence microscopy
DAPI
Claudin-5
ZO1
Merge
Day 3
Day 5
Day 7
Day 12
b
STORM microscopy
Post-confluence (<7 days)
Super-confluence (>11 days)
ZO1
Claudin-5
c
Simulation of claudin-5 clustering
Post-confluence
Super-confluence
d
Post- confluence
Super-confluence
Number of signals/cluster
Cluster area (µm²)
e
Cluster density (signals/µm²)
*
Post-confluence
Super-confluence

Fig. 1: Super-resolution microscopy of endothelial tight junctions. *In vitro* process of TJ maturation is accompanied by TJ architectural changes characterized by the formation of smaller, denser and more discrete clusters of TJ proteins. **a,** Epi-fluorescent imaging of claudin-5 (green) and ZO1 (red) immunostaining of bEND.3 cells in indicated time points after the cultures reached confluence state. Note translocation of claudin-5 from cytoplasmic localizations into continuous lines around the boundaries of the cells (known as 'strands'), along the *in vitro* maturation process. Scale bars, 10 μm and 5 μm in insets. **b,** dSTORM imaging (Gaussian visualization) of claudin-5 (green) and ZO1 (red) immunostaining of bEND.3 cells confluent monolayers. TJ proteins form bead-like structures, especially in the super-confluence state. Claudin-5 signals are more concentrated in discrete and shorter foci (flanking ZO1 signals, arrowheads, right) than in the post-confluence state (arrows, left). During maturation TJ proteins translocate from different cellular locations (left) almost exclusively into the lateral cell membranes (right). Scale bar, 1 μm. **c,** Examples of dSTORM imaging simulation of claudin-5 in bEND.3 cells used for quantifications of clustering properties (produced by a custom clustering Matlab code, see methods for details). Signals were defined to be clustered if their 2D location was smaller than 70 nm threshold distance. Cluster pattern visualization showing all points that belong to the same cluster with the same identifying color. **d,** Quantifications of claudin-5 clustering properties showed a shift towards smaller clusters with more claudin-5 signals per cluster at the super-confluence state. Clusters with higher numbers of signals were more abundant at this late state, especially in clusters with area smaller than 0.3 μm^2. **e,** Average claudin-5 cluster density was ~4-fold higher at the super-confluence state than in the post-confluence state (n=183 clusters (post-confluence) and 281 clusters (super-confluence) in 5 independent experiments). Data are mean±s.e.m. *P < 0.05 (Two tailed Mann–Whitney U-test).

We further investigated nano-architectural changes in the *in vitro* context of claudin-5 expression and tight junction function. In line with previous publications (Koto et al., 2007), we could confirm that total claudin-5 protein levels in bEND.3 cells rise with time in culture (Fig. S1a). Nevertheless, we found that in general, bEND.3 monolayer trans-endothelial electrical resistance (TEER) is relatively low (~40-100 Ωxcm2). Therefore, we turned to an alternative *in vitro* system that presents substantially superior barrier features with pronounced TJ function and TEER levels closer to those estimated for the *in vivo* levels: human iPSC differentiation into brain microvascular endothelial-like cells (iBMECs) (Lippmann, Al-Ahmad, Azarin, Palecek, & Shusta, 2014; Lippmann et al., 2012; Vatine et al., 2017; Vatine et al., 2019). In our culturing conditions TEER levels started at ~500-1000 Ωxcm2 already a day after seeding. We monitored TEER and upon a noticeable elevation of approximately an additional ~1000 Ωxcm2 (2-3 days in culture), we measured claudin-5 protein levels with western blot, permeability in transwells, and in parallel imaged cultures with STORM (Fig 2). We noticed that TJ function was improving, with TEER elevation (Fig. 2a, S1b) and flux decrease (Fig. 2b), but could not detect noticeable changes in claudin-5 protein levels. STORM imaging revealed that only clustered organization of claudin-5 could be found in these cells (Fig. 2c), and that pronounced change in nano-scale organization of claudin-5 clusters could be observed; clusters were smaller in area and denser (Fig. 2d-f) along with improvement in TJ function. The majority of cluster areas were smaller than 0.1 μm^2, and the average signal density (per cluster) was higher with elevated TEER (~2.3-fold, Fig. 1f, $P< 0.01$). In general, clusters of claudin-5 are much denser in iBMECs compared to bEND.3 cells (~8 fold denser), which correlates with differences in TEER.

Altogether, we suggest that the *in vitro* process of TJ maturation is accompanied by TJ nano-architectural changes characterized by the formation of smaller, denser and more discrete clusters of TJ proteins.

Figure 2

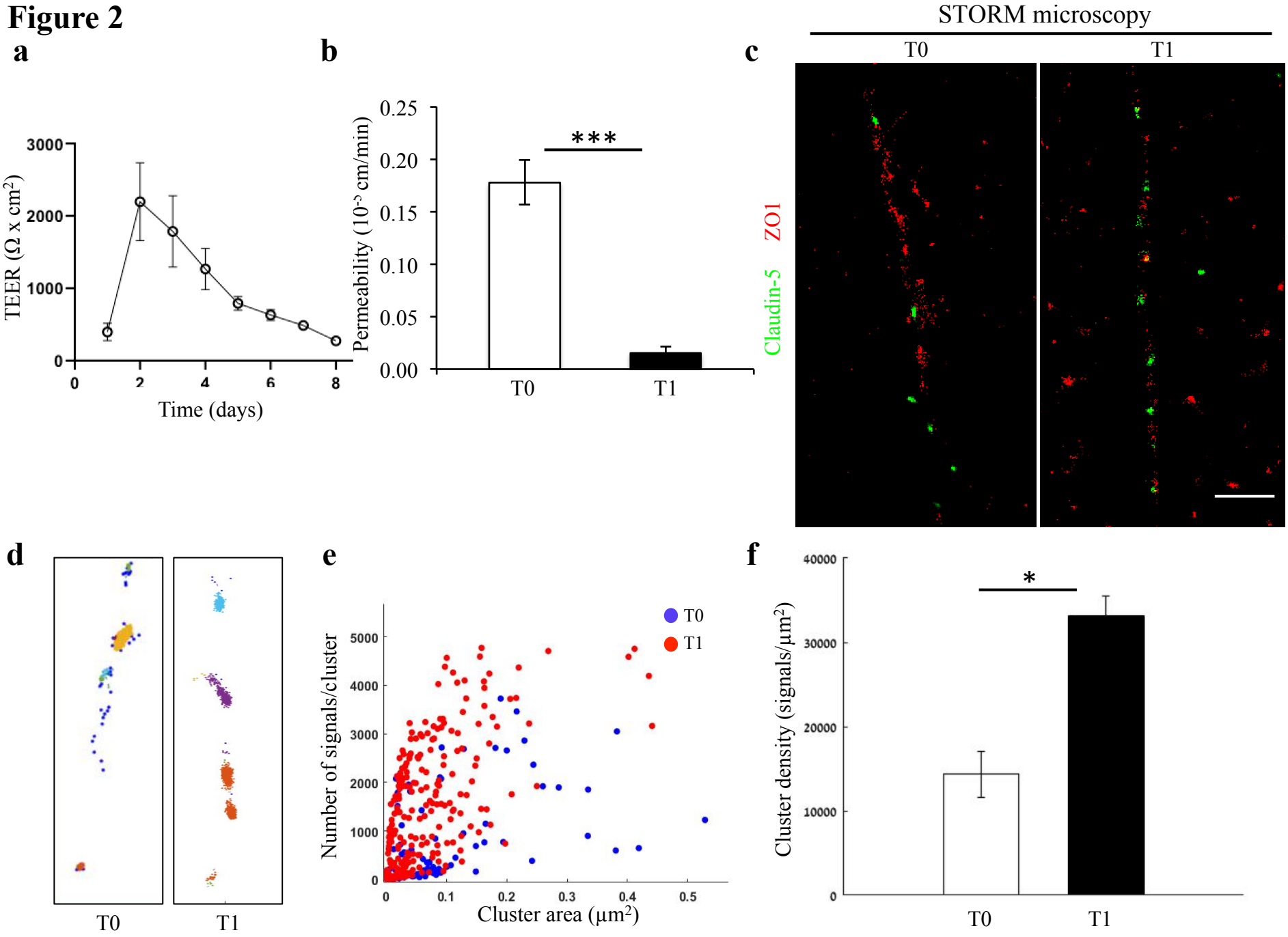
a
TEER (Ω x cm²)
3000
2000
1000
0
0
2
4
6
8
Time (days)
b
Permeability (10⁻⁵ cm/min)
0.25
0.20
0.15
0.10
0.05
0.00
***
T0
T1
c
STORM microscopy
T0
T1
ZO1
Claudin-5
d
T0
T1
e
Number of signals/cluster
5000
4000
3000
2000
1000
0
0
0.1
0.2
0.3
0.4
0.5
Cluster area (µm²)
T0
T1
f
Cluster density (signals/µm²)
40000
30000
20000
10000
0
*
T0
T1

Fig. 2: Changes in nano-scale architecture correlates with tight junction function. Enhanced TJ function is accompanied by formation of smaller and denser clusters of claudin-5. **a,** Enhanced TJ function demonstrated by increase in TEER, along the first days of induced human brain microvascular endothelial-like cell (iBMEC) culture (n=4 experiments/12 inserts. TEER here shows data of a representative experiment. For average change in TEER across all experiments see Supplementary Figure S1b. n=4 inserts for permeability). **b,** Enhanced TJ function demonstrated by reduced permeability to sodium fluorescein (T0 represents low TEER and T1 represents high TEER states, n=4 inserts). Data are mean ± SD. *** P<0.0003 (two tailed pair t- test). **c,** dSTORM imaging (Gaussian visualization) of claudin-5 (green) and ZO1 (red) immunostaining in iBMEC confluent monolayers. Claudin-5 signals are concentrated in discrete and short foci at both time points. Scale bar, 1 μm. **d,** Examples of dSTORM imaging simulation of claudin-5 in iBMECs used for quantifications of clustering properties (produced by a custom clustering Matlab code, see methods for details). Cluster pattern visualization showing all points that belong to the same cluster with the same identifying color. **e,** Quantifications of claudin-5 clustering properties showed a shift towards smaller clusters with more claudin-5 signals per cluster along the improvement in TJ function. **f,** Average claudin-5 cluster density more than doubled (from 14,341 to 33,141 signals/μm^2) with the improvement in TJ function (n=90 clusters (in lower TEER) and 278 clusters (in higher TEER) in triplicate cultures of two independent experiments). Data are mean ± s.e.m. *P < 0.01 (two tailed Mann–Whitney U-test).

192 **Molecular organization of mouse cortical BBB TJs**

193 To determine if the organization of TJ components observed *in vitro* occurs also in the
194 brain, we developed a technique that enabled dSTORM imaging of BBB TJ in brain tissue
195 sections (see methods for details). First we used fluorescent circulating tracers (Fig. 3b) and
196 co-staining of claudin-5 together with the endothelial-specific transcription factor ERG (Fig.
197 3c) and showed that claudin-5 dSTORM signals are exclusively localized to vascular
198 structures. We found that similar to the *in vitro* data, claudin-5 exhibits clustered organization
199 also *in vivo*, demonstrated in both cross and sagittal sections of cortical capillaries (of post-
200 natal mice, Fig. 4b). The considerably improved resolution of dSTORM imaging could be
201 appreciated when compared to epi-fluorescent images at very high magnifications of the same
202 capillary, under the same microscope settings (Fig. 4b, 5a).
203

Figure 3

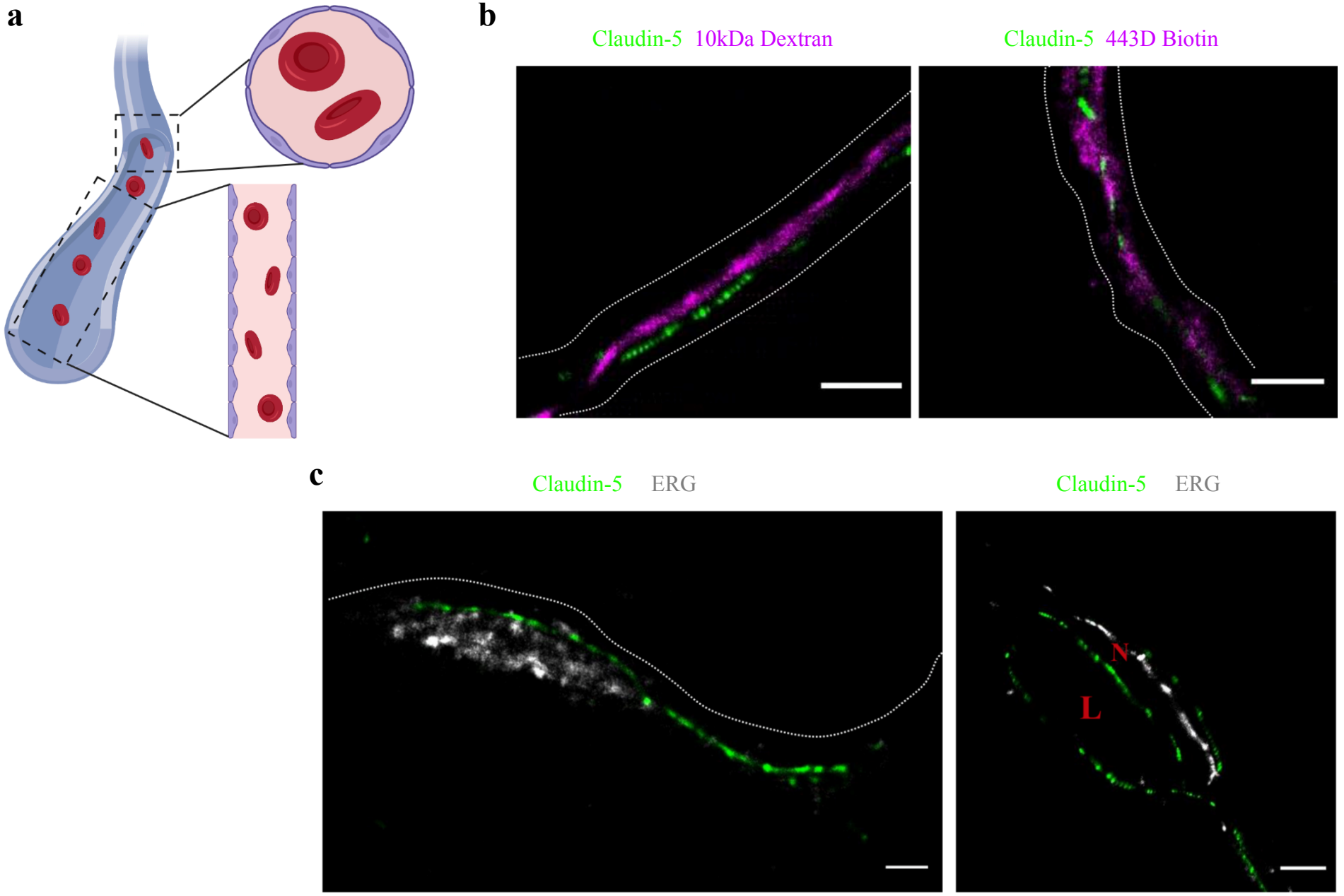
a
b
Claudin-5 10kDa Dextran
Claudin-5 443D Biotin
c
Claudin-5 ERG
Claudin-5 ERG
N
L

Fig. 3: Claudin-5 signals in dSTORM imaging are exclusively localized to vascular structures. dSTORM imaging in cortical fixed tissue sections of post-natal day 9 mice. **a,** Illustration of a vascular structure with cross versus sagittal section directions, and the projected orientation of endothelial cells contact points. **b,** Claudin-5 staining (green) together with fluorescent circulating tracers (10 kDa dextran, and ~443 Dalton sulfo-NHS-biotin, magenta) are used to demarcate sagittal views of elongated vessels (dashed line, Scale bars, 1 μm). **c,** Staining for claudin-5 (green) together with the endothelial-specific transcription factor ERG (gray) showing capillary cross and sagittal sections (Scale bars, 1 μm). L – capillary lumen, N – endothelial nucleus. $n>30$ capillaries.

Figure 4

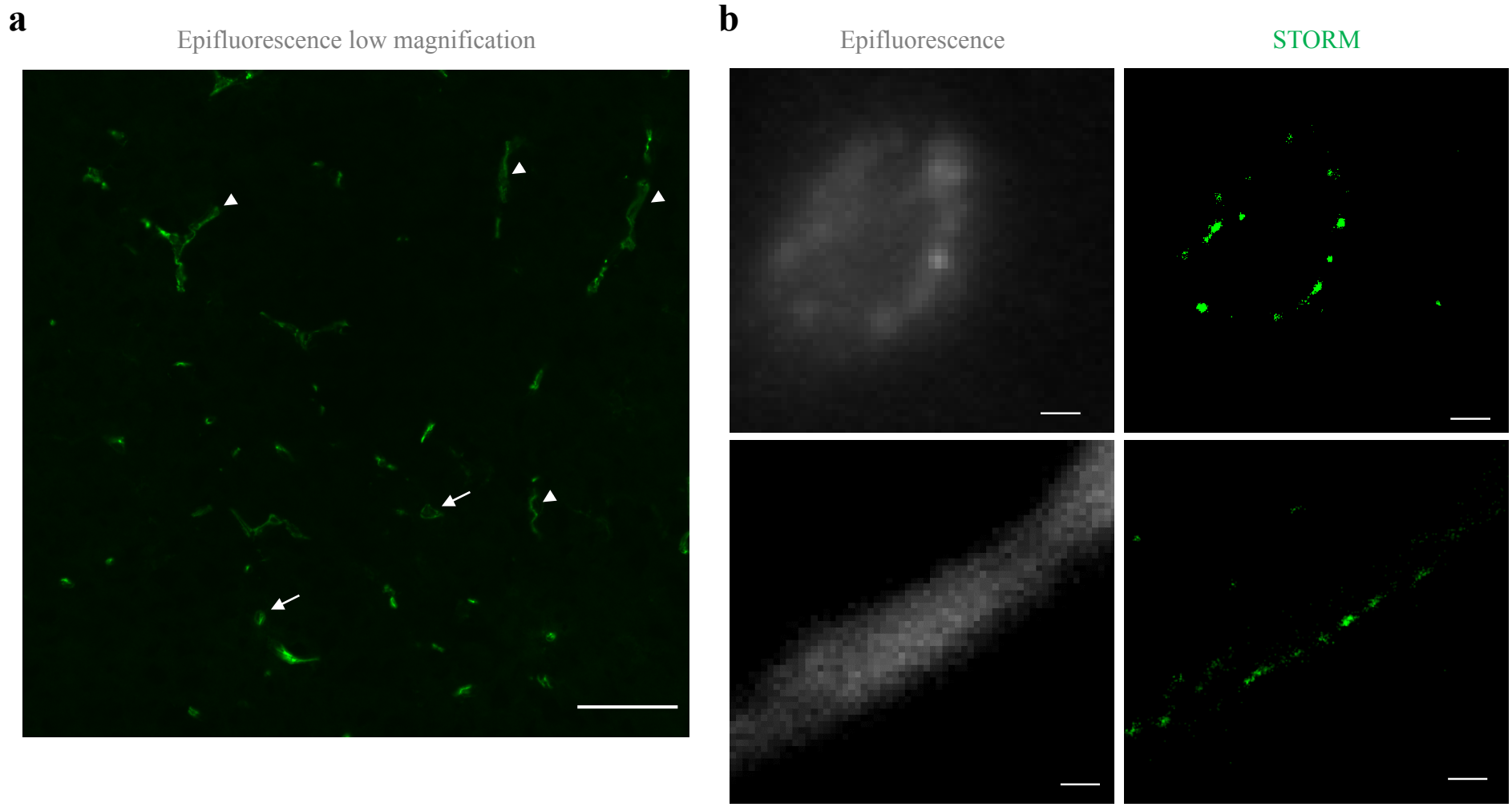
a
Epifluorescence low magnification
b
Epifluorescence
STORM

Fig. 4: Claudin-5 exhibits clustered organization in cortical capillaries. Imaging in cortical fixed tissue sections of post-natal day 9 mice. **a,** Low magnification view of claudin-5 staining imaged by epi-fluorescent microscopy showing vascular fragments in cross-sections (arrows) or in sagittal-sections (arrowheads, scale bar, 50 μm). **b,** Claudin-5 exhibits clustered organization *in vivo;* dSTORM (right) compared to epi-fluorescent images (left) of claudin-5 immunostaining in P9 cortical capillary cross-section (upper panel) or sagittal- section (lower panel) (scale bars, 1 μm), n>30 capillaries.

Embryonic and post-natal development of the BBB provides an opportunity to investigate *in vivo* TJs maturation; as cortical capillaries acquire their restrictive barrier properties along a gradual developmental process (Ben-Zvi et al., 2014; Butt, Jones, & Abbott, 1990; Daneman, Zhou, Kebede, & Barres, 2010; Hagan & Ben-Zvi, 2015; Langen et al., 2019; Saunders, Liddelow, & Dziegielewska, 2012; Sohet et al., 2015). From mouse embryonic day 12 (E12) until E15, we and others have previously shown that the newly formed cortical capillaries have not yet acquired their full restrictive barrier properties (Ben-Zvi et al., 2014; Daneman et al., 2010). We therefore compared claudin-5 organization at E12 and at post-natal day 9 (P9) by analyzing cellular abundance and clustering properties (Fig 5, S2). We assumed that E12 capillaries had a more defused claudin-5 appearance with longer clusters (Fig. 5a, arrow), but further analysis revealed that these were composed of many small clusters with relatively small gaps between them (example of the two types of clustering simulations, Fig. S2a). Claudin-5 clustering properties analysis showed that there were about 2.6 times more discrete clusters per capillary at E12 than at P9 (657 *vs*. 246 clusters in a set of 20 capillaries of each age, Fig. 5b). Capillary diameter was also significantly larger in E12 than in P9 (Fig 5a,c; 11.1±0.47 μm and 5.9±0.39 μm respectively (mean±s.e.m), P<0.0001), which might explain the difference in numbers of clusters per capillary.

239 Distribution of claudin-5 clusters area in E12 capillaries was skewed towards smaller
240 clusters (with no dramatic difference between the distributions, Fig. 5b). There was no
241 dramatic difference also in the distribution of signals per cluster (Fig. 5b) or signal densities
242 between the two groups (Fig. S2b). Thus there were no obvious changes in claudin-5
243 clustering properties that correlated with changes in TJs maturation.

244 In addition to changes in capillary diameter the total number of claudin-5 signals per
245 capillary was significantly higher in E12 than at P9 ($14{,}341 \pm 1{,}257$ and $3{,}590 \pm 372$
246 respectively (mean±s.e.m), $P<0.0001$, Fig. 5c). Normalizing the total number of signals per
247 capillary to its diameter (displayed as 'Normalized cellular Claudin-5', Fig. 5c,d) resulted in a
248 similar significant difference (Fig. 5d). Based on this result we suggest that the total cellular
249 amount of claudin-5 is not a strong predictor of TJ functionality. Our conclusion relates to the
250 developmental and early post-natal BBB (reflected in our data), which might be distinct from
251 the adult BBB.
252

Figure 5

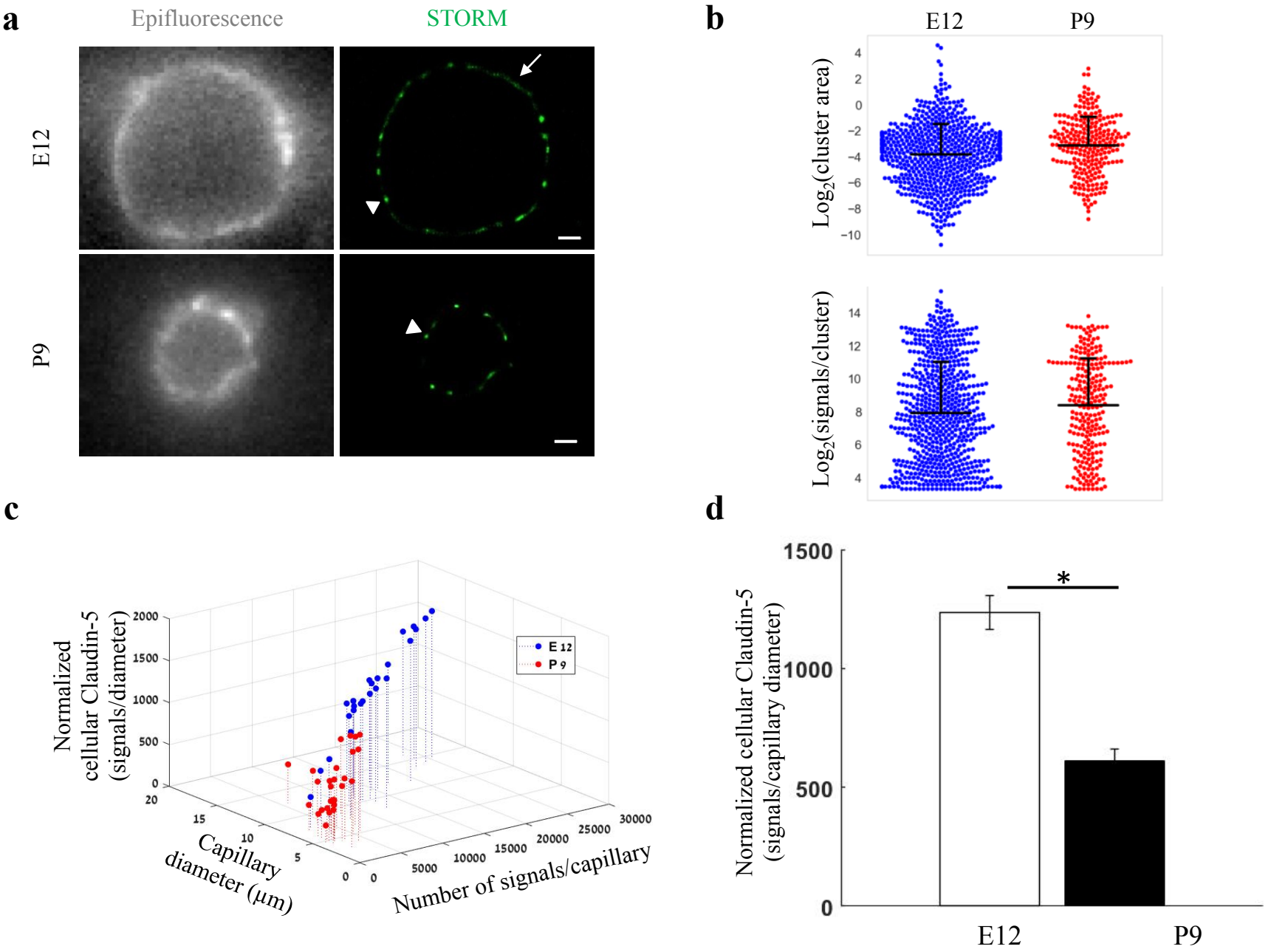
a
Epifluorescence
STORM
E12
P9
b
E12
P9
Log2(cluster area)
Log2(signals/cluster)
c
Normalized cellular Claudin-5 (signals/diameter)
E 12
P 9
Capillary diameter (μm)
Number of signals/capillary
d
Normalized cellular Claudin-5 (signals/capillary diameter)
*
E12
P9

Fig. 5: Total cellular claudin-5 abundance does not correlate with BBB restrictive properties. Quantifications of claudin-5 levels and clustering properties along developmental BBB maturation **a,** dSTORM (right) compared to epi-fluorescent images (left) of claudin-5 immunostaining in E12 and P9 cortical capillary cross-sections. Two distinct claudin-5 organizations could be observed; discrete clusters (arrowheads) and a more defused claudin-5 appearance composed of many small clusters with relatively small gaps between them, evident only in E12 capillaries (arrow, see Extended Data Fig. S1a for further analysis). Scale bars, 1 μm. **b,** Claudin-5 clustering-properties analysis showed that there were about 2.6 times more discrete clusters per capillary at E12 than at P9 (a set of 20 capillaries of each age). Distribution of claudin-5 clusters area in E12 capillaries was skewed towards smaller clusters and the average cluster area was slightly smaller in E12 with no dramatic difference between the distributions (average of 0.309 μm^2 (E12) vs. 0.3413 μm^2 (P9). There was no dramatic difference in the distribution of signals per cluster or signal densities between the two groups (see Fig. S1b). *n*=3 pups/embryos, 20 capillaries, 657 clusters (E12) and 246 clusters (P9). Data are mean±s.e.m. **c,** Quantifications of total cellular claudin-5 per capillary cross section shows a shift towards lower claudin-5 levels and smaller capillary diameter in P9 than in E12 vasculature. Capillary diameter was significantly smaller (5.9±0.39 μm (P9), 11.1±0.47μm (E12)), total number of claudin-5 signals per capillary was significantly lower (3,590±372 (P9), 14,341±1,257 (E12)). **d,** Normalizing the total number of signals per capillary to its diameter shows the average claudin-5 cellular abundance is significantly lower at P9. *n*=25 capillaries (E12) and 27 capillaries (P9) of 3 embryos/pups. Data are mean±s.e.m. *P < 0.05 (Two tailed Mann–Whitney U-test).

We then expanded the structural and organizational properties examination to include additional TJ proteins in cortical capillaries. Imaging ZO1 and occludin showed that like claudin-5, ZO1 had clustered organization (Fig. 6a left), whereas occludin was much less organized in discrete clusters and had more dispersed organization patterns (Fig. 6a right). Based on published biochemical studies, ZO1 is known to physically interact with the C-terminals of both claudin-5 and occludin, which aligns with our imaging data demonstrating signals of all three in close proximity (Fig. 6, S3).

While each capillary cross-section presented multiple claudin-5 clusters, we assumed that not all claudin-5 proteins are localized to TJs. Indeed we could detect claudin-5 clusters in close proximity with a lysosomal marker (LAMP1, Fig. S4a), suggesting lysosome localization. In addition, we could detect claudin-5 clusters in close proximity with an ER marker (BiP, Fig. S4b), suggesting ER localization. Therefore we focused on structures where claudin-5 and ZO1 clusters were coupled (Fig. 6b arrows), reasoning that these might better reflect actual TJs. We analyzed the density of claudin-5 signals in clusters that were coupled with ZO1 clusters and compared it to the density of claudin-5 signals in independent clusters (Fig. 6b, arrowhead) of both E12 and P9 (Fig. 6b,c). The average density of P9 claudin-5 clusters that were coupled with ZO1 clusters was about five-fold higher ($P<0.0215$) than in independent claudin-5 clusters. The average density of E12 claudin-5 clusters was similar regardless of proximity to ZO1 clusters, and was low compared to P9 independent claudin-5 clusters. We concluded that claudin-5 clusters in TJs (based on pairing with ZO1) have higher claudin-5 density in late developmental stages, a structural feature that correlates with BBB maturation.

Figure 6

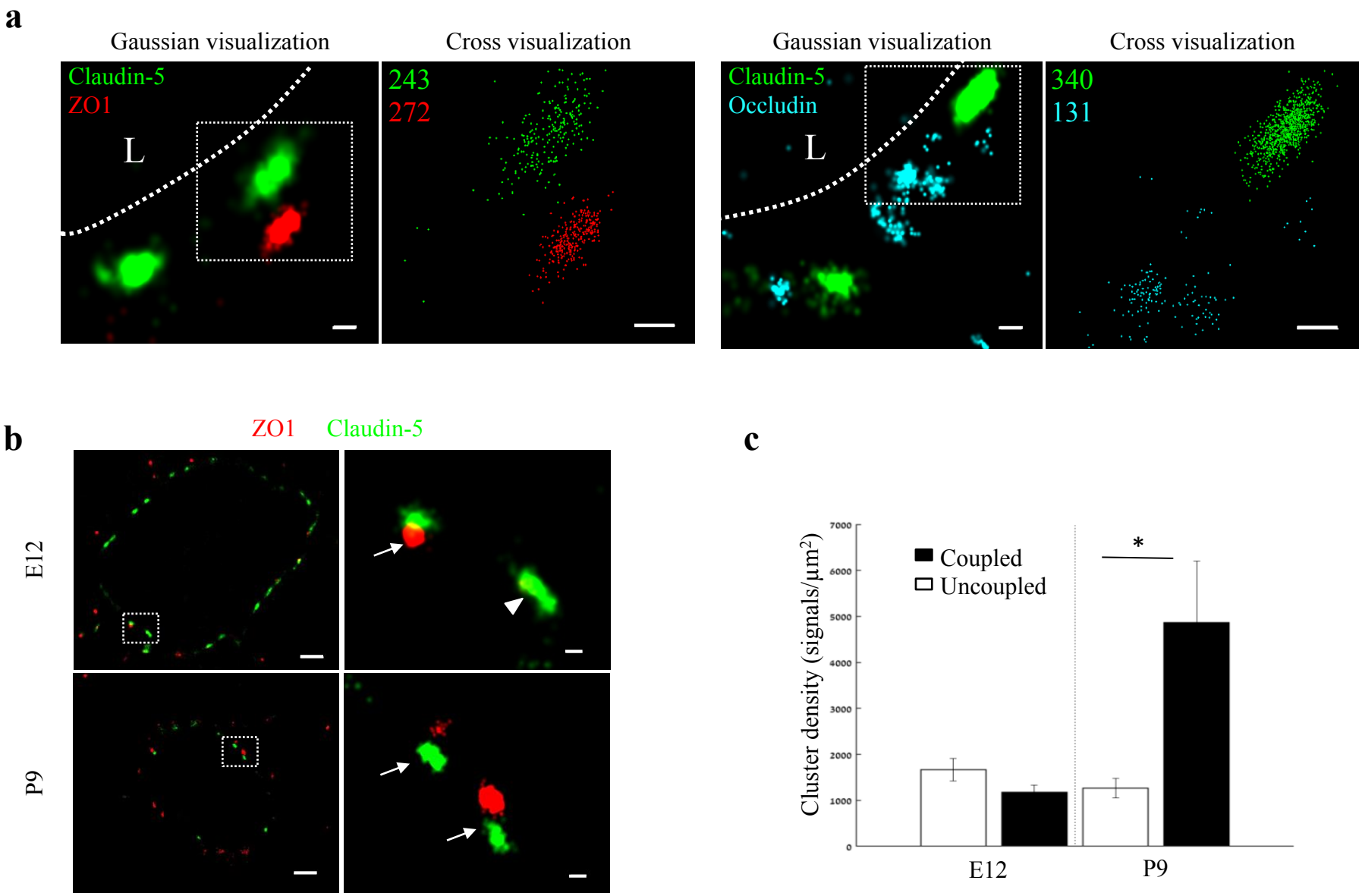
a
Gaussian visualization
Cross visualization
Gaussian visualization
Cross visualization
Claudin-5
ZO1
L
243
272
Claudin-5
Occludin
L
340
131
b
ZO1
Claudin-5
E12
P9
c
Coupled
Uncoupled
*
Cluster density (signals/μm²)
7000
6000
5000
4000
3000
2000
1000
0
E12
P9

Fig. 6: Molecular organization of mouse cortical BBB TJs. Nano-scale molecular organization of TJ proteins in cortical capillaries of postnatal wild-type mice (P9). **a,** Claudin-5 and ZO1 display clustered organization (left) whereas occludin was much less organized in discrete clusters and had more dispersed organization patterns (right). 2D-STORM imaging data demonstrates that signals of all three TJ proteins are in close proximity ('Gaussian visualization' in which signal intensity correlates with localization precision). An inset with magnifications of each cluster (right images) demonstrates the very high molecular density of TJ proteins ('Cross visualization' shows all resolved signals where each single-molecule signal displays as a cross). Scale bars, 100 nm. Representative signal numbers are shown. *n*=40 capillaries of 4 wild-type pups. L – capillary lumen. **b,** dSTORM imaging (Gaussian visualization) of claudin-5 (green) and ZO1 (red) immunostaining of E12 and P9 cortical capillary cross-sections. Note that some claudin-5 clusters are coupled with ZO1 clusters (high magnification insets, arrows) while some are independent claudin-5 clusters (arrowhead). Scale bars, 1 μm and 100 nm in insets. **c,** Average density of P9 claudin-5 clusters that were coupled with ZO1 clusters was ~5-fold higher than independent claudin-5 clusters. The average density of E12 claudin-5 clusters was similar regardless of proximity to ZO1 clusters, and was low compared to P9 independent claudin-5 clusters. *n*=40 clusters from 11 capillaries and 43 clusters from 11 capillaries (of 3 embryos/pups, P9 and E12 respectively). Data are mean±s.e.m. *P < 0.05 (Two tailed Mann–Whitney U-test).

316 **ZO1 clustering is independent of claudin-5 *in-vivo***

317 In order to gain insights on mechanisms underlying Nano-scale molecular architecture of
318 BBB TJs, we imaged claudin-5 null and wild-type littermates cortical capillaries with
319 dSTORM. This approach was intended to enable testing whether claudin-5 being a very
320 abundant transmembrane TJ component might be an organizer of other TJ components. We
321 initially confirmed the specificity of claudin-5 antibodies, with no detectable staining in null
322 tissue (confocal microscopy of E16 cortical null and wild-type littermates' tissues, Fig. 7a).
323 Specificity was also confirmed with dSTORM imaging (Fig. 7b). Finally, we found that
324 absence of claudin-5 did not altered, ZO1 clustering organization nor it had any effect on
325 occludin dispersed organization patterns (Fig 7c). In contrary to the previous conclusions of
326 unaltered molecular composition of claudin-5 null TJs (Nitta et al., 2003), quantification of
327 dSTORM imaging revealed that the total cellular occludin levels (normalized to capillary
328 circumference) were higher in claudin-5 null capillaries by ~1.29 fold compared to occludin
329 levels in wild-type capillaries ($P<0.0039$, Fig. 7d). Overall cellular ZO1 expression levels
330 were also higher in claudin-5 null capillaries (not statistically significant). These new findings
331 of molecular alterations in TJ protein levels in the claudin-5 null BBB demonstrate the high
332 sensitivity provided by single molecule super resolution imaging, with these molecular
333 changes most probably obscured when tested by other approaches. We concluded that nano-
334 scale organization of both ZO1 and occludin are independent of claudin-5 expression (at least
335 in the embryonic setting). We also believe that these findings warrant a new evaluation of
336 claudin-5 function at BBB junctions.

Figure 7

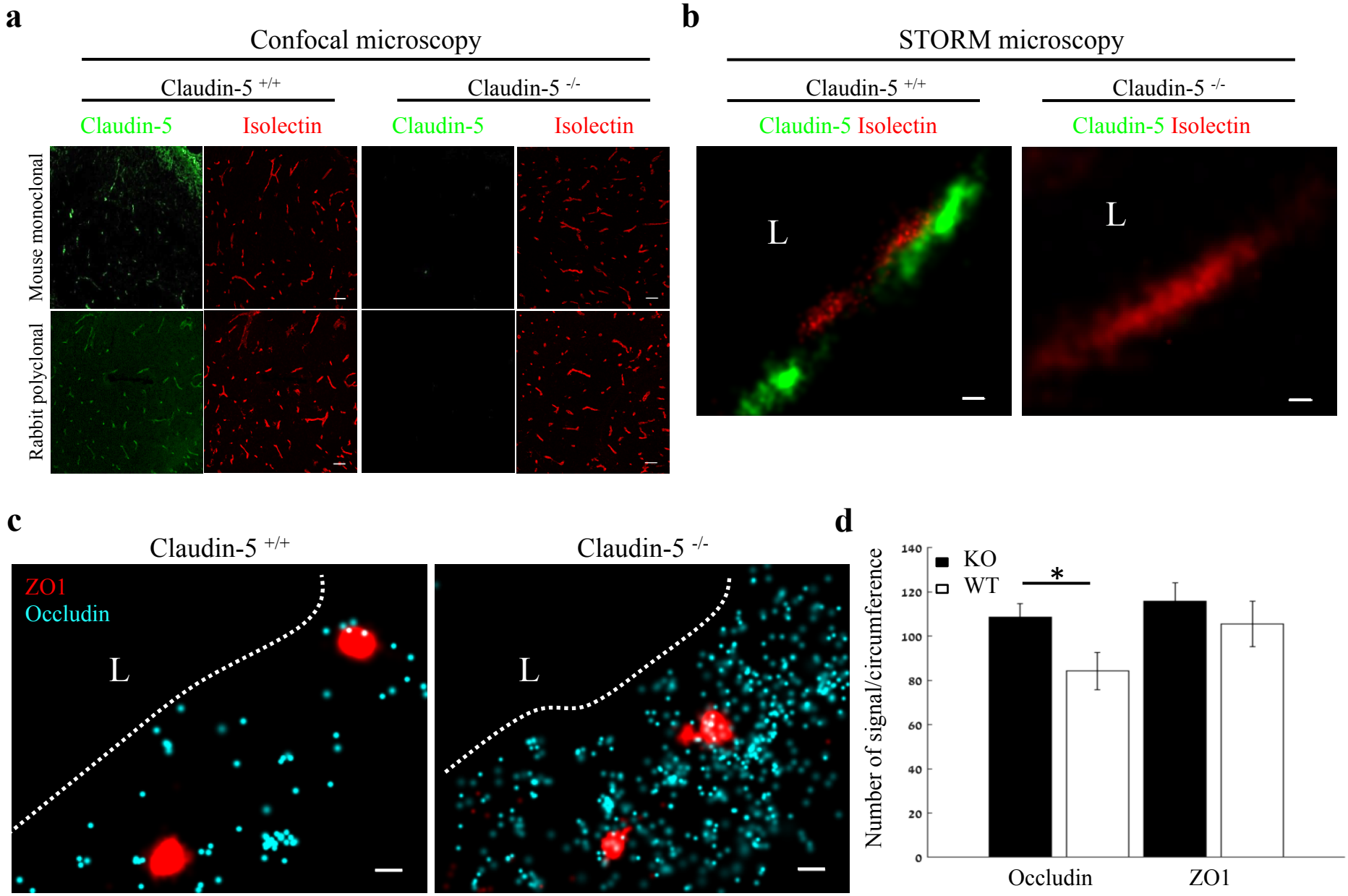
a
Confocal microscopy
Claudin-5 +/+
Claudin-5 -/-
Claudin-5
Isolectin
Claudin-5
Isolectin
Mouse monoclonal
Rabbit polyclonal
b
STORM microscopy
Claudin-5 +/+
Claudin-5 -/-
Claudin-5 Isolectin
Claudin-5 Isolectin
L
L
c
Claudin-5 +/+
Claudin-5 -/-
ZO1
Occludin
L
L
d
Number of signal/circumference
KO
WT
*
0
20
40
60
80
100
120
140
Occludin
ZO1

Fig. 7: Nano-scale organization of both ZO1 and occludin are independent of claudin-5 expression. a-b, Claudin-5 antibodies specificity was confirmed by both confocal microscopy (**a,** Scale bars, 50 μm) and dSTORM microscopy (**b,** Scale bars, 0.1 μm), with no detectable staining in E16 cortical null tissues (Isolectin staining used to localize vasculature, *n*=4 wild-type, 4 claudin-5 null embryos). **c,** E16 claudin-5 null and wild-type littermates cortical capillaries imaged with dSTORM display unaltered ZO1 clustering organization and occludin dispersed organization patterns. Scale bars, 100 nm. **d,** Total cellular signal quantifications revealed that occludin levels were ~1.29-fold higher in claudin-5 null capillaries compared to wild-type. Total cellular ZO1 signal levels were also higher in claudin-5 null capillaries (not statistically significant). Data are mean±s.e.m. *P < 0.05 (Two tailed Mann–Whitney U-test). L – capillary lumen. *n*=109 capillaries of 4 wild-type embryos and 86 capillaries of 4 claudin-5 null embryos.

Investigating BBB TJ function using super-resolution microscopy

In light of the identified maturation changes in claudin-5 clustering properties, we sought to directly test TJ function *in vivo*. To this end we employed tracer challenges and compared TJs permeability at three developmental time points (E12, E16 and P9, Fig. 8). We performed dSTORM imaging of cortical capillaries following injection of fluorescent tracers to the blood stream and used claudin-5 immunofluorescence to demarcate capillary boundaries and localize TJs in cortical tissues. Similar to the traditional HRP/EM approach (Reese & Karnovsky, 1967), dSTORM imaging enables detection of functional BBB TJs with the added value of TJ protein visualization and localization relative to tracer molecules. The HRP/EM approach is not compatible in young embryos and therefore until now, dysfunction of immature TJs was only speculated to underlie capillary hyper-permeability at early stages of BBB development. Thus we tested E12 TJ function with an *in utero* embryonic liver tracer

injection method that we previously developed to assess BBB permeability during early mouse developmental stages (Ben-Zvi et al., 2014). As expected from previous experiments with conventional microscopy (Ben-Zvi et al., 2014), with dSTORM imaging we could confirm that E12 capillaries did not restrict movement of tracer molecules across the BBB (Fig. 8a; 10-kDa dextran, upper left. ~443 Dalton sulfo-NHS-biotin, lower left). Tracer signals could be detected in the basal side or further away, presumably in brain tissue (Fig. 8, arrowheads). Moreover, we could directly image TJs contribution to this leakage; tracer signals were found intermingled with claudin-5 clusters (Fig. 8, arrows) and in many cases we could detect tracer signals in three locations relative to claudin-5 clusters: the luminal side, the cluster area itself and the abluminal side. We interpreted these as direct evidence of tracer leakage across immature TJs. As expected, mature P9 capillaries restrict movement of the vast majority of tracer molecules (Fig. 8; 10-kDa dextran, upper right. ~443 Dalton sulfo-NHS-biotin, lower right) from the lumen to the basal side (similar results were obtained using Biocytin, data not shown).

In order to examine TJ function along the developmental axis, we also imaged E16 TJs. First, we validated that at E16 cortical TJs were indeed restrictive to the 10-kDa tracers (aligned with general permeability that we previously demonstrated (Ben-Zvi et al., 2014)). TJs at this stage were functional and prevented tracer leakage across claudin-5 clusters (Fig. 8a, middle-upper). Surprisingly, the smaller tracer, sulfo-NHS-biotin, was not restricted to the vessels' lumen, and was evident also on the brain side (Fig. 8a middle-lower, arrowheads). Therefore at this stage TJs were not as mature as P9 TJs and did not prevent smaller tracer leakage across claudin-5 clusters. These developmental changes in permeability are reflected in quantification of tracer signal density at the abluminal side of the junctions (Fig. 8b,c). We conclude that BBB TJs might have different maturation time courses for different size

386 selectivity properties and that the dSTORM approach is suitable for in depth investigations of

387 this phenomena in future studies.

Figure 8

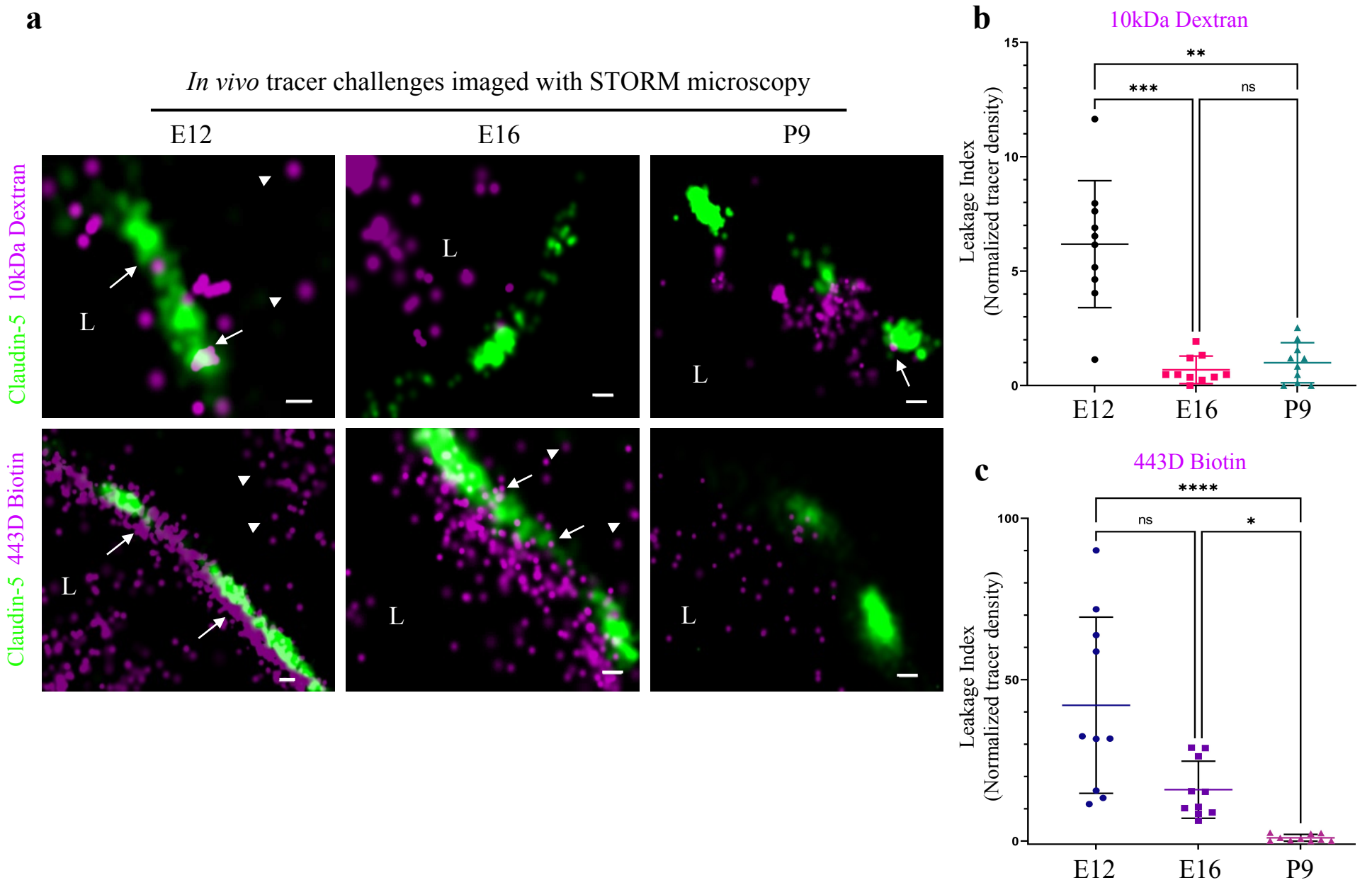
a
In vivo tracer challenges imaged with STORM microscopy
E12
E16
P9
Claudin-5 10kDa Dextran
Claudin-5 443D Biotin
L
b
10kDa Dextran
Leakage Index
(Normalized tracer density)
15
10
5
0
**
***
ns
E12
E16
P9
c
443D Biotin
Leakage Index
(Normalized tracer density)
100
50
0
****
ns
*
E12
E16
P9

Fig. 8: Investigating BBB TJ function using super-resolution microscopy. Tracer challenges testing cortical capillaries permeability with dSTORM imaging, provides evidence of leakage across immature TJs. **a,** E12 TJ function tested with an *in utero* embryonic liver tracer injection method (Ben-Zvi et al., 2014). 10 kDa dextran signals (upper-left) and ~443 Dalton sulfo-NHS-biotin signals (lower-left) were found in the luminal side, intermingling with claudin-5 clusters (arrows) and in the abluminal side and further away (presumably brain tissue, arrowheads). These were interpreted as evidence of tracer leakage across immature TJs. Following trans-cardiac tracer challenges, dSTORM imaging shows P9 capillaries can restrict movement of tracer molecules from the lumen to the brain side (10 kDa dextran upper-right, and ~443 Dalton sulfo-NHS-biotin lower-right). E16 cortical capillaries were previously found to prevent leakage of 10-kDa tracers (Ben-Zvi et al., 2014; Licht, Dor-Wollman, Ben-Zvi, Rothe, & Keshet, 2015), also validated here with dSTORM imaging (middle-upper). Surprisingly, at this stage sulfo-NHS-biotin was not restricted to the vessels' lumen, evident also on the brain side (middle-lower arrowheads) and intermingling with claudin-5 clusters (arrows). Scale bars, 100 nm. L – capillary lumen. *n*=40 capillaries for each tracer of 3 pups/embryos. **b-c**, Developmental changes in permeability are reflected in quantification of tracer signal density at the abluminal side of the junctions (10 kDa dextran at b, and 443 Dalton sulfo-NHS-biotin at c). Relative leakage index was calculated as tracer signal density (signals/area) in a fixed area and distance from the abluminal side of the claudin-5 signal, and was normalized to the average signal density at P9 (set as leakage index=1). *n*=10 capillaries for each tracer of 3 pups/embryos, *P<0.0123, **P<0.0031 ,***P<0.0006, ****P<0.0001, Kruskal-Wallis test and Dunn's test for multiple comparisons.

Discussion

We present here a new super resolution imaging approach for BBB research. Using this approach we revealed novel structural and functional features of BBB TJs through examination of TJ maturation of EC cultures, normal cortical mouse BBB development and claudin-5 null embryos. With super-resolution imaging we could overcome the limitations of conventional microscopy, which is essential for BBB TJ investigations since it provides proper spatial resolution and enables sensitive quantifications of TJ proteins and tracer molecules.

We provide direct evidence of non-functional TJs in the early embryonic BBB. HRP-EM approaches were not useful for studying early embryonic stages; consequently direct evidence for the cellular pathway mediating leakage in early embryogenesis was missing. A recent mouse retina-vasculature study showed that developmentally, the TJ pathway is already restrictive before the vesicular pathway is blocked (Chow & Gu, 2017) and studies in sheep demonstrated similar trends in the brain (Dziegielewska et al., 1979). We suggest that in mouse cortical vasculature, the course of barrier-genesis might be different. We found that there are different TJ maturation developmental time-courses for different size selectivities. Thus, even in later stages (E16), when vesicular activity is clearly diminished at the BBB (based on ultra-structural EM studies (Bauer et al., 1993)), we found that TJs were not fully mature and mediate leakage of a low molecular-weight tracer.

We focused on three major TJs components and found sparse occluding vs. clustered ZO1/claudin-5 molecular architecture. Since our current study did not include additional TJ components, we could not differentiate in our analyses between subtypes of TJs and therefore these might represent claudin-5 presumably localized to either bicellular or tricellular junctions.

434 TJ claudin-5 shifted into denser cluster organization along with *in vivo* BBB maturation,
435 a finding which is in line with freeze-fracture EM data that suggested cluster organization of
436 EC TJs (Haseloff et al., 2015; Morita et al., 1999). Therefore, we suggest that confocal
437 imaging description of claudin-5 strands might be a misrepresentation of actual claudin-5
438 organization. Notably, dSTORM might give rise to some artificial clustering due to antibody
439 staining and fluorophore overcounting (Burgert, Letschert, Doose, & Sauer, 2015). Hence,
440 our clustering results of claudin-5 and ZO1 should be taken as relative changes in protein
441 organization under the different tested conditions. In addition, our imaging included multiple
442 stains (two different antibodies used for claudin-5 and testing several different fluorophores
443 conjugated to secondary antibody combinations, all resulted in similar clustering data).
444 Moreover, occludin did not show similar clustering properties and finally, we used algorithms
445 to minimize fluorophore overcounting (see Methods (Ovesny, Krizek, Borkovec, Svindrych,
446 & Hagen, 2014)).
447 Previous TJ studies primarily investigated epithelial cells, which have considerably larger
448 volumes than ECs. These studies emphasized a contentious organization of transmembrane
449 proteins along the apical circumference of the cells, providing 'sealing belts'. Our finding of
450 disrupted lines with discrete clusters, forming bead-like structures does not support the
451 concept that claudin-5 fully construct these 'sealing belts'. We can think of three possible
452 explanations for this discrepancy; first, we cannot exclude that our staining approach
453 underrepresents the entire claudin-5 localizations (highly compacted foci might reduce
454 antibodies accessibility). Second, TJ cleft directionality is variable especially *in vivo* and the
455 3D organization of the 'sealing belt' might be missed once imaged in 2D. This explanation is
456 incomplete especially once examining the *in vitro* data where very flat coordinated orientation
457 monolayers are imaged at the cell-glass contacts. Third and most exciting possibility is that
458 other TJ proteins (yet to be discovered) occupy the gaps between claudin-5 clusters; these

might be coordinately localized to complete the 'sealing belts'. Such theory aligns with the findings that the claudin-5 null BBB has only partially perturbed sealing properties (Nitta et al., 2003).

Our data supports the huge cellular claudin-5 abundance reported by other approaches (e.g average of ~12,000 transcripts per capillary endothelial cell (Vanlandewijck et al., 2018), average of ~14,000 (E12) or ~3500 (P9) signals per cross section in our data). Total levels of junctional proteins/transcripts are presented in many studies (measured by western blot, conventional imaging, qPCR/RNAseq etc. (Armulik et al., 2010; Daneman et al., 2010; Nitta et al., 2003; Vanlandewijck et al., 2018; Y. Zhang et al., 2014)), and down regulation of these components are often used as an indicator for TJ dysfunction (Alvarez et al., 2011; Bell et al., 2010; Bell et al., 2012; Zhong et al., 2008). Our findings that claudin-5 expression inversely correlates with BBB tightness in the developmental setting might be distinct from the situation in the adult BBB. Similar to our findings, dSTORM imaging of cultured alveolar epithelial cell TJs, shows increase claudin-5 in response to alcohol exposure together with an increase in paracellular leak (Schlingmann et al., 2016). In pathological settings a minimal threshold of claudin-5 expression might result in TJ leakage. Thus, it will be interesting to test if such a threshold is breached in disease (as suggested for the 22q11 syndrome (Greene et al., 2018)).

The differential size selectivity we found in E16 was reminiscent of the seminal study by Nitta *et al*. (Nitta et al., 2003) demonstrating that the BBB of E18.5 claudin-5 null mouse embryos was hyper-permeable to Hoechst (562 Dalton) and to gadolinium (~742 D) but not to 10 KDa dextran or to endogenous albumin (~66 KDa). Following this study, claudin-5 was considered the molecular component of BBB TJs responsible for restricting passage of low molecular weight substances (<800 D). Our data indicates that despite the presence of claudin-5, TJs of E16 wild-type mice display similar differential size selectivity as E18.5

484 claudin-5 null TJs. Accordingly it seems that claudin-5 is not the sole component responsible
485 for restricting passage of low molecular weight substances.

486 Further investigations are needed in order to evaluate the possible redundancy between
487 different BBB TJ proteins. The increase in occludin expression we describe for claudin-5 null
488 TJ could reflect a developmental compensatory mechanism that might obscure the full
489 contribution of claudin-5 to TJ function. Nitta *et al*. also suggested that in the absence of
490 claudin-5, claudin-12-based TJs in brain vessels would function as a molecular sieve
491 restricting high molecular weight substances but allowing low molecular weight substances
492 (<800 kDa) to leak into the brain. Recent RNAseq data indicated low expression of claudin-
493 12 in BBB endothelium (approximately 80 fold lower then claudin-5 (Vanlandewijck et al.,
494 2018; Y. Zhang et al., 2014)), reports farther corroborated by a claudin-12 reporter mouse
495 study indicating expression in many other CNS cell types (Castro Dias et al., 2019).

496 Our findings of unchanged cluster organization of ZO1 in the absence of claudin-5 might
497 be explained by interaction of ZO1 with other TJ proteins (other than occludin which is not
498 clustered) or by recent reports of ZO1 capability of self-organization into membrane-attached
499 compartments via phase separation that can drive TJ formation in epithelia cells (Beutel,
500 Maraspini, Pombo-Garcia, Martin-Lemaitre, & Honigmann, 2019). It also aligns with
501 claudin-5 null embryos having no overt morphological abnormalities (Nitta et al., 2003). The
502 other two ZO proteins might also participate in formatting TJ architecture. Based on
503 scRNAseq data, ZO3 is not expressed at the BBB but ZO2 has lower but significant mRNA
504 levels (Vanlandewijck et al., 2018). It would be interesting to explore ZO2 nano-scale
505 organization as it shares the same self-organization capacity as ZO1 and therefore might
506 display similar clustering properties (Beutel et al., 2019).

507 Further development of the BBB dSTORM approach will provide additional insights: the
508 ability to image proteins together with membrane lipids and 3D reconstruction of super-

509 resolution imaging are both important focus points for future studies. Deciphering BBB TJ
510 biology with this new approach will aid in evaluating the potential of TJ manipulation for
511 drug delivery and in identifying TJ abnormalities in disease.
512
513 **Methods**
514 **Animals.** ICR (CD-1®, Envigo, Rehovot, Israel) mice were used for embryonic and post-
515 natal BBB functionality assays and dSTORM imaging. Pregnant mice were obtained
516 following overnight mating (day of vaginal plug is defined as embryonic day 0.5). All
517 animals were housed in SPF conditions and treated according to institutional guidelines
518 approved by the Institutional Animal Care and Use Committee (IACUC) at Hebrew
519 University.
520 The claudin-5 mutant mice (Nitta et al., 2003) were kindly provided by Dr. Mikio Furuse
521 (National Institute for Physiological Sciences, Japan). Mice were housed in individually
522 ventilated cages under specific pathogen-free conditions at 22 °C with free access to chow and
523 water. E16 claudin-5 wild-type and null embryos were obtained according to procedures
524 approved by the Veterinary Office of the Canton Bern, Switzerland. Claudin-5 null mutant
525 and wild-type embryos were genotyped using lysates prepared from tips of tails using the
526 following 3 PCR primers: Cldn5_UPS: GCCCCTACTAGGACAGAAACTGGTAG;
527 Cldn5_REV1: CAGACCCAGAATTTCCAACGCTGC and PGK-pA-FW1:
528 GCCTGCTCTTTACTGAAGGCTCTT, which provide a 422 bp product for the claudin-5
529 wild-type allele and a 630 bp product for the claudin-5-knockout allele. PCR cycling
530 conditions were: 4 min. 94°C; 1 min. each at 94°C, 64°C and 72°C; repeated 35 times and a
531 final 5 min elongation step at 72°C.
532 **Tissue preparation.** After dissection, brains were placed in 4% paraformaldehyde (PFA,
533 Sigma Aldrich) at 4°C overnight, cryopreserved in 30% sucrose and frozen in TissueTek

OCT (Sakura). Frozen brains were cut to 5-8 µm slices for immunofluorescent staining (CM1950, Leica) to produce coronal brain sections.

Immunohistochemistry. Tissue sections or cell cultures were blocked with 20% goat serum and 20% horse serum, permeabilized with 0.5% Triton X-100, and stained with primary and secondary antibodies (see antibodies table for details). Sample were mounted with freshly made imaging buffer for dSTORM (describe in the dSTORM imaging section) and visualized by dSTORM and epifluorescence, or mounted in Fluoromount G (EMS) and visualized by confocal microscopy. Both a polyclonal and a monoclonal anti-claudin-5 antibody were found to be highly specific in dSTORM, validated with claudin-5 null mice staining, as in confocal imaging (Fig. 7a,b).

Epitope	Class	Host	Catalogue number	Company	Dilution
* Claudin 5	Monoclonal	Mouse	35-2500	Life Technologies	1:100
** Claudin 5	Polyclonal	Rabbit	1600 34	Zymed	1:50
ZO1/TJP1	Polyclonal	Rabbit	61-7300	Thermo Fisher Scientific	1:200
Occludin	Monoclonal	Mouse	33-1500	Thermo Fisher Scientific	1:50
ERG	Monoclonal	Rabbit monoclonal	ab92513/ EPR3864	abcam	1:200
Lamp1	Monoclonal	Rat	ID4B	DSHB/ AB_528127	1:200
BiP	Monoclonal	Rabbit	C50B12 #3177	Cell Signaling Technology	1:100
GAPDH	Monoclonal	Rabbit	ab181602	abcam	1:400

Fluorophore	Isotype	Catalogue number	Company	Dilution
Alexa fluor®647	Anti-rabbit IgG	711-605-152	Jackson	1:1000
Alexa fluor®647	Anti-mouse IgG	711-605-151	Jackson	1:1000
Alexa fluor®568	Anti-rabbit IgG	A11011	Life Technologies	1:1000
Alexa fluor®568	Anti-mouse IgG	A1103-1	Life Technologies	1:1000
Alexa fluor®488	Anti-mouse IgG	715-545-151	Jackson	1:1000
Streptavidin Alexa fluor®647	Biotin	S32357	Molecular Probes	1:800
Alexa fluor®647	Anti-rat IgG	712-605-153	Jackson	1:1000

Embryonic BBB permeability assay. We used the method we developed and fully described in our previous publication (Ben-Zvi et al., 2014). In brief, dams were deeply anesthetized with ketamine-xylazine i.p. (8.5 mg/ml ketamine, 1.5 mg/ml xylazine, in 100 µl saline). Embryos were injected with 5 µl of Dextran, Alexa Fluor®647 anionic fixable (D22914, Molecular Probes, 2 mg/ml) or 5 µl of EZ-Link™ Sulfo-NHS-Biotin (21217, Thermo Fisher Scientific, 1 µg/20 µl), while still attached via the umbilical cord to the mother's blood circulation. Taking advantage of the sinusoidal, fenestrated and highly permeable liver vasculature, dye was injected using a Hamilton syringe into the embryonic liver and was taken up into the circulation in a matter of seconds. After 5 min of circulation, embryonic heads were fixed by 4 hours immersion in 4% PFA at 4°C, cryopreserved in 30% sucrose and frozen in TissueTek OCT (Sakura).

Postnatal BBB permeability assay. P9 pups were deeply anaesthetized and 10 µl of Dextran, Alexa Fluor®647 anionic fixable (D22914, Molecular Probes, 2 mg/ml) or EZ-Link™ Sulfo-NHS-Biotin (21217, Thermo Fisher Scientific, 1 µg/20 µl), were injected into the left ventricle with a Hamilton syringe. After 5 min of circulation, brains were dissected and fixed by immersion in 4% PFA at 4°C overnight, cryopreserved in 30% sucrose and frozen in

565 TissueTek OCT (Sakura).

566 **Cell culture.** The mouse brain endothelioma cell line (bEnd.3) was purchased from American
567 Type Culture Collection (Manassas, VA, USA). bEnd.3 cells were cultured with Dulbecco's
568 Modified Eagle's medium high glucose (DMEM), supplemented with 10% fetal bovine serum
569 and 1% penicillin-streptomycin solution (Biological Industries, Beit HaEmek, Israel). Cells
570 were incubated at 37°C in a humid atmosphere in the presence of 5% CO2. Cells at passages
571 26-27 were suspended (0.25% Trypsin EDTA B, Biological Industries) and seeded on 24 mm
572 precision coverslips (no. 1.5H, Marienfeld-superior, Lauda-Königshofen, Germany). Cells
573 were washed with PBS and fixed with 4% PFA (at indicated time point; up to 7 days or more
574 than 11 days post-confluence).

575 **iPSC differentiation to brain microvascular endothelial-like cells (iBMECs).** iPSCs from
576 a healthy individual (BGUi012-A) (Falik et al., 2020) were cultured between passages 10-17,
577 seeded on Matrigel (Corning) with daily replacement of NutriStem medium (Biological
578 Industries) as previously described ((Falik et al., 2020), PMID: 32905996). iPSCs were
579 passaged every 6-7 days with Versene (Life Technologies) at a 1:12 ratio. Differentiation into
580 iBMECs was carried out as previously described (Jagadeesan, Workman, Herland, Svendsen,
581 & Vatine, 2020; Vatine et al., 2017; Vatine et al., 2019); cells were passaged and cultured for
582 2–3 days until reaching a density of 2-3x10^5 cells/well. Next, medium was replaced with
583 unconditioned medium without bFGF [UM/F: 200 mL of DMEM/F12 (1:1) (Gibco), 50 mL
584 knock-out serum replacement (Gibco), 2.5 mL non-essential amino acids (Gibco), 1.25 mL of
585 gluta-max (Gibco), 3.8 uL of β-mercapto-ethanol (Sigma), and 2.5 mL PSA (BI)] and
586 changed daily for six days. Medium was then replaced with human endothelial serum-free
587 medium (hESFM, Life Technologies) supplemented with 20 ng/mL bFGF and 10 mM All-
588 trans retinoic acid (RA) (Sigma) (Biomedical Technologies, Inc.) for 2 days. Cells were then
589 gently dissociated into single cells with Accutase (StemPro) and plated in hESFM medium at

a density of 1×10^6 cells on transwells (0.4 µm pore size; Corning), coverslips or petri dishes that were pre-coated with a mixture of collagen IV (400 ug/mL; Sigma) and fibronectin (100 ug/mL; Sigma).

TEER measurements. Trans-endothelial electrical resistance (TEER) was measured every 24 h following iBMEC seeding. Resistance was recorded using an EVOM ohmmeter with STX2 electrodes (World Precision Instruments). TEER values were presented as Ωxcm2 following the subtraction of an empty transwell and multiplication by 1.12 cm^2 to account for the surface area. TEER measurements were measured three independent times for each sample and at least twice for each experimental condition.

Paracellular permeability measurements. Sodium fluorescein (10 mM) was added to the upper chamber of the Transwells. Aliquots (100 µl) were collected from the bottom chamber every 15 min and replaced with fresh medium. Fluorescence (485 nm excitation and 530 nm emission) was quantified at the end of the experiment with a plate reader. Rate of tracer accumulation was used to calculate Pe values was as previously described (Vatine et al., 2017). Monolayer fidelity was confirmed at the beginning and at the end of each experiment by TEER measurements.

iBMECs STORM imaging. iBMECs were seeded on 24 mm precision coverslips (no. 1.5H, Marienfeld-Superior, Lauda-Königshofen, Germany), pre-coated with a mixture of collagen IV (400 ug/mL; Sigma) and fibronectin (100 ug/mL; Sigma). Cultures were fixed in 4% paraformaldehyde for 20 min at room temperature (RT), washed three times with PBS and kept in 4°C until processing.

Western blot analysis. Whole cell extracts were isolated using RIPA buffer (50 mM Tris pH 7.4, 150 mM NaCl, 5 mM EDTA pH 8.0, and 1% Nonidet-P40) supplemented with protease inhibitors (Roche). The concentration of the isolated proteins was determined using Bradford

reagent (Sigma). 30-50 micrograms of the protein were separated on a 15% polyacrylamide gel and electrophoretically transferred to PVDF membranes (Millipore). Membranes incubated with the primary antibodies against claudin-5 (1:1000 ,Zymed 1600-34) or GAPDH (1:400, ab181602, ABCAM)) and the appropriate secondary antibodies.

dSTORM imaging. We used a dSTORM system, which allows imaging at approximately 20 nm resolution by using photo-switchable fluorophores (all dSTORM imaging was done on TIRF mode). 5 μm brain slices were mounted on poly-D-lysine coated coverslips (no. 1.5H, Marienfeld-superior, Lauda-Königshofen, Germany). dSTORM imaging was performed in a freshly prepared imaging buffer containing 50 mM Tris (pH 8.0), 10 mM NaCl and 10% (w/v) glucose with an oxygen-scavenging GLOX solution (0.5 mg/ml glucose oxidase (Sigma-Aldrich), 40 μg/ml catalase (Sigma-Aldrich), 10 mM cysteamine MEA (Sigma-Aldrich) and 1% β mercaptoethanol (Barna et al., 2016; Dempsey, Vaughan, Chen, Bates, & Zhuang, 2011; J. Zhang, Carver, Choveau, & Shapiro, 2016). A Nikon Ti-E inverted microscope was used. The N-STORM Nikon system was built on TIRF illumination using a 1.49 NA X100 oil immersion objective and an ANDOR DU-897 camera. 488, 568 and 647 nm laser lines were used for activation with cycle repeat of ~8000 cycles for each channel. Nikon NIS Element software was used for acquisition and analysis; analysis was also performed by ThunderSTORM (NIH ImageJ (Ovesny et al., 2014)). Images in 2D were Gaussian fit of each localization; in the N-STORM software.

dSTORM quantifications. The dSTORM approach we used is based on labeling the target protein with a primary antibody and then using a secondary antibody conjugated to a fluorophore. Thus resolved signals represent a location that is approximately 40 nm from the actual epitope (assuming the approximation of the two antibodies' length in a linear conformation). The number of signals represents an amplification of the actual target numbers. Amplification corresponds to the primary antibody in the case of a polyclonal

antibody (assuming binding to several epitopes in the same protein, which could be reduced by the use of monoclonal antibodies). Amplification also corresponds to several secondary antibodies binding to a single primary antibody and to several fluorophores attached to a single secondary antibody. Nevertheless, resolution of approximately 20 nm allows us to separate signals and to use these as proxies to the abundance of target molecules, which can reliably be used to compare different states.

Cellular expression level quantifications: We defined the capillary cross-section as an endothelial unit and quantified claudin-5 signals within capillary cross-sections as proxy to total cellular claudin-5 expression levels.

Cluster area, signal numbers and signal densities: Single molecule localization microscopy (SMLM) results in point patterns having specific coordinates of individual detected molecules. These coordinates are typically summarized in a 'molecular list' (provided by ThunderSTORM analysis (NIH ImageJ) (Ovesny et al., 2014)). In order to define molecular clusters, we analyzed the molecular lists through a custom Matlab code (MathWorks) using the Matlab functions "Cluster" and "Linkage", as follows: First, our code calculated distances between each point and all other points in the point pattern of the SMLM image. Then, we set a distance threshold for defining molecules that belong to the same cluster: two points were defined to be clustered if their distance was smaller than the threshold distance (e.g. 70 nm). All points that were clustered with a specific point belong to one cluster (as defined by linkage function). Hence, a point could only be within one cluster. The code then defined and saved the properties of each cluster, such as the area of the cluster, the number of points within the cluster, and the number of clusters. Cluster densities were calculated as number of points divided by each cluster area. Finally, the point patterns were visualized, while showing all points that belong to the same cluster with the same identifying color (Fig. 1c, S1). The 70 nm threshold distance used for quantifications was determined based on the following

parameters: minimal distance could not be below 40 nm (see above antibody labeling strategy); BBB TJs covering continuous contact points, as we evaluated in published TEM imaging data, range approximately up to 100 nm; simulation of claudin-5 density in clusters, measured in different threshold distances between 50-100 nm did not yield significant differences (Fig. S3).

Confocal imaging. Images were captured using Nikon Eclipse Ni confocal microscope, objective X20 with Nikon C2 camera and Nis-Elements software. Images are maximal z-projection of optical sections taken from a 12µm tissue section imaged with 0.85 µm intervals.

Epi-Fluorescence microscopy. Images presented in Figures 1a, 4a, were taken using an Olympus BX51, 10X/0.3 and 20X/0.5, with Andor Zyla camera, and Nikon NIS elements software (version D4.5) for both image acquisition and analysis.

Statistical analysis. All comparisons were performed by two-tailed Mann–Whitney U-tests, or by two tailed pair t- test (as indicated in the figure legends), $P<0.05$ was considered significant (GraphPad Prism 8.0.1(244) for Windows, GraphPad Software, San diego, California, USA). For multiple comparisons of leakage index (Figure 8), the Kruskal-Wallis test and Dunn's tests for multiple comparisons were used. For the comparison between post confluence and super confluence we used cluster densities across experiments, for the comparison between ZO1 paired and unpaired claudin-5 clusters we used cluster densities across experiments, for comparisons related to capillaries diameter and total claudin-5 levels we used capillaries across experiments and for comparisons of total occludin levels in wild-type and caludin-5 null embryos we used capillaries across experiments (for exact repetitions see figure legends). Sample size for all immunofluorescence experiments was determined empirically using standards generally employed by the field: a minimum of three animals per group in each experiment, a minimum of four tissue sections of each tissue and a minimum of

689 10 capillaries per group. In the data set of claudin-5 null and control littermates, the person
690 collecting the data and analyzing was blind to the animal's genotype.

691 **Acknowledgments**

692 We would like to thank; Mss. Sivan Gelb, Kian Atamny and Victoria Miller of the Ben-
693 Zvi group for scientific and writing inputs, Drs. Avihu Klar and Danny Ben-Zvi for scientific
694 inputs, Dr. Gillian Kay for valuable scientific editing, Dr. Norman Grover for his helpful
695 advice regarding statistical analyses, and Ms. Yaara Arad for help with data presentation. This
696 study was supported by the Leona M. and Harry B. Helmsley Charitable Trust (2015PG-
697 ISL007); and the Israel Science Foundation (grants 1882/16 and 2402/16) to ABZ, the Swiss
698 National Science Foundation (grant 1890809) to BE and the Israel Science Foundation (grant
699 1621/18) and the Ministry of Science and Technology, Israel (grant 3-15647) to GDV.
700 We wish to dedicate this work to the memory of Prof. Morris J. Karnovsky of Harvard
701 Medical School, a scientific giant and pioneer of the BBB research field. We are grateful for
702 his mentorship and scientific support, and especially for encouraging us to pursue our
703 endeavor of super resolution imaging of BBB TJs.

704 **Contribution**

705 ESa performed the majority of the experiments together with RD, SA, BB, MZ and UD.
706 ABZ and ESa conceived the project and designed the experimental plan. ESa, SA and ABZ
707 wrote this manuscript, with BE, RD, OY, ESh, GDV and BB, reviewing and contributing to
708 writing. OY wrote custom Matlab codes for dSTORM analyses; ESh provided critical
709 scientific guidance for dSTORM imaging and analyses. UD and BE supported claudin-5 null
710 mouse strain experiments. MZ and GV preformed iBMEC experiments. RD supported the
711 development of imaging methods and the establishment of the dSTORM imaging system.

712 **Ethics declarations**

713 Competing interests

714 The authors declare no competing interests.
715

References

Alvarez, J. I., Dodelet-Devillers, A., Kebir, H., Ifergan, I., Fabre, P. J., Terouz, S., . . . Prat, A. (2011). The Hedgehog pathway promotes blood-brain barrier integrity and CNS immune quiescence. *Science, 334*(6063), 1727-1731. doi:10.1126/science.1206936

Armulik, A., Genove, G., Mae, M., Nisancioglu, M. H., Wallgard, E., Niaudet, C., . . . Betsholtz, C. (2010). Pericytes regulate the blood-brain barrier. *Nature, 468*(7323), 557-561. doi:10.1038/nature09522

Barna, L., Dudok, B., Miczan, V., Horvath, A., Laszlo, Z. I., & Katona, I. (2016). Correlated confocal and super-resolution imaging by VividSTORM. *Nat Protoc, 11*(1), 163-183. doi:10.1038/nprot.2016.002

Bauer, H. C., Bauer, H., Lametschwandtner, A., Amberger, A., Ruiz, P., & Steiner, M. (1993). Neovascularization and the appearance of morphological characteristics of the blood-brain barrier in the embryonic mouse central nervous system. *Brain Res Dev Brain Res, 75*(2), 269-278. doi:10.1016/0165-3806(93)90031-5

Bauer, H. C., Krizbai, I. A., Bauer, H., & Traweger, A. (2014). "You Shall Not Pass"-tight junctions of the blood brain barrier. *Front Neurosci, 8*, 392.

Bell, R. D., Winkler, E. A., Sagare, A. P., Singh, I., LaRue, B., Deane, R., & Zlokovic, B. V. (2010). Pericytes control key neurovascular functions and neuronal phenotype in the adult brain and during brain aging. *Neuron, 68*(3), 409-427.

Bell, R. D., Winkler, E. A., Singh, I., Sagare, A. P., Deane, R., Wu, Z., . . . Zlokovic, B. V. (2012). Apolipoprotein E controls cerebrovascular integrity via cyclophilin A. *Nature, 485*(7399), 512-516.

Ben-Zvi, A., Lacoste, B., Kur, E., Andreone, B. J., Mayshar, Y., Yan, H., & Gu, C. (2014). Mfsd2a is critical for the formation and function of the blood-brain barrier. *Nature, 509*(7501), 507-511. doi:10.1038/nature13324

Beutel, O., Maraspini, R., Pombo-Garcia, K., Martin-Lemaitre, C., & Honigmann, A. (2019). Phase Separation of Zonula Occludens Proteins Drives Formation of Tight Junctions. *Cell, 179*(4), 923-936 e911. doi:10.1016/j.cell.2019.10.011

Brightman, M. W., & Reese, T. S. (1969). Junctions between intimately apposed cell membranes in the vertebrate brain. *J Cell Biol, 40*(3), 648-677. doi:10.1083/jcb.40.3.648

Burgert, A., Letschert, S., Doose, S., & Sauer, M. (2015). Artifacts in single-molecule localization microscopy. *Histochem Cell Biol, 144*(2), 123-131. doi:10.1007/s00418-015-1340-4

Butt, A. M., Jones, H. C., & Abbott, N. J. (1990). Electrical resistance across the blood-brain barrier in anaesthetized rats: a developmental study. *J Physiol, 429*, 47-62.

Castro Dias, M., Coisne, C., Baden, P., Enzmann, G., Garrett, L., Becker, L., . . . Engelhardt, B. (2019). Claudin-12 is not required for blood-brain barrier tight junction function. *Fluids Barriers CNS, 16*(1), 30.

Chow, B. W., & Gu, C. (2017). Gradual Suppression of Transcytosis Governs Functional Blood-Retinal Barrier Formation. *Neuron, 93*(6), 1325-1333 e1323.

Daneman, R., Zhou, L., Kebede, A. A., & Barres, B. A. (2010). Pericytes are required for blood-brain barrier integrity during embryogenesis. *Nature, 468*(7323), 562-566. doi:10.1038/nature09513

Dempsey, G. T., Vaughan, J. C., Chen, K. H., Bates, M., & Zhuang, X. (2011). Evaluation of fluorophores for optimal performance in localization-based super-resolution imaging. *Nat Methods, 8*(12), 1027-1036.

763 Dziegielewska, K. M., Evans, C. A., Malinowska, D. H., Mollgard, K., Reynolds, J. M.,
764 Reynolds, M. L., & Saunders, N. R. (1979). Studies of the development of brain
765 barrier systems to lipid insoluble molecules in fetal sheep. *J Physiol, 292*, 207-231.
766 Falik, D., Rabinski, T., Zlotnik, D., Eshel, R., Zorsky, M., Garin-Shkolnik, T., . . . Vatine, G.
767 D. (2020). Generation and characterization of iPSC lines (BGUi004-A, BGUi005-A)
768 from two identical twins with polyalanine expansion in the paired-like homeobox 2B
769 (PHOX2B) gene. *Stem Cell Res, 48*, 101955. doi:10.1016/j.scr.2020.101955
770 Furuse, M., Fujita, K., Hiiragi, T., Fujimoto, K., & Tsukita, S. (1998). Claudin-1 and -2:
771 novel integral membrane proteins localizing at tight junctions with no sequence
772 similarity to occludin. *J Cell Biol, 141*(7), 1539-1550.
773 Furuse, M., Hirase, T., Itoh, M., Nagafuchi, A., Yonemura, S., Tsukita, S., & Tsukita, S.
774 (1993). Occludin: a novel integral membrane protein localizing at tight junctions. *J*
775 *Cell Biol, 123*(6 Pt 2), 1777-1788.
776 Greene, C., Kealy, J., Humphries, M. M., Gong, Y., Hou, J., Hudson, N., . . . Campbell, M.
777 (2018). Dose-dependent expression of claudin-5 is a modifying factor in
778 schizophrenia. *Mol Psychiatry, 23*(11), 2156-2166.
779 Hagan, N., & Ben-Zvi, A. (2015). The molecular, cellular, and morphological components of
780 blood-brain barrier development during embryogenesis. *Semin Cell Dev Biol, 38*, 7-
781 15. doi:10.1016/j.semcdb.2014.12.006
782 Haseloff, R. F., Dithmer, S., Winkler, L., Wolburg, H., & Blasig, I. E. (2015).
783 Transmembrane proteins of the tight junctions at the blood-brain barrier: structural
784 and functional aspects. *Semin Cell Dev Biol, 38*, 16-25.
785 doi:10.1016/j.semcdb.2014.11.004
786 Jagadeesan, S., Workman, M. J., Herland, A., Svendsen, C. N., & Vatine, G. D. (2020).
787 Generation of a Human iPSC-Based Blood-Brain Barrier Chip. *J Vis Exp*(157).
788 doi:10.3791/60925
789 Kealy, J., Greene, C., & Campbell, M. (2018). Blood-brain barrier regulation in psychiatric
790 disorders. *Neurosci Lett*, 133664. doi:10.1016/j.neulet.2018.06.033
791 Knowland, D., Arac, A., Sekiguchi, K. J., Hsu, M., Lutz, S. E., Perrino, J., . . . Agalliu, D.
792 (2014). Stepwise recruitment of transcellular and paracellular pathways underlies
793 blood-brain barrier breakdown in stroke. *Neuron, 82*(3), 603-617.
794 Koto, T., Takubo, K., Ishida, S., Shinoda, H., Inoue, M., Tsubota, K., . . . Ikeda, E. (2007).
795 Hypoxia disrupts the barrier function of neural blood vessels through changes in the
796 expression of claudin-5 in endothelial cells. *Am J Pathol, 170*(4), 1389-1397.
797 Langen, U. H., Ayloo, S., & Gu, C. (2019). Development and Cell Biology of the Blood-
798 Brain Barrier. *Annu Rev Cell Dev Biol, 35*, 591-613. doi:10.1146/annurev-cellbio-
799 100617-062608
800 Licht, T., Dor-Wollman, T., Ben-Zvi, A., Rothe, G., & Keshet, E. (2015). Vessel maturation
801 schedule determines vulnerability to neuronal injuries of prematurity. *J Clin Invest,*
802 *125*(3), 1319-1328.
803 Liebner, S., Dijkhuizen, R. M., Reiss, Y., Plate, K. H., Agalliu, D., & Constantin, G. (2018).
804 Functional morphology of the blood-brain barrier in health and disease. *Acta*
805 *Neuropathol, 135*(3), 311-336.
806 Lippmann, E. S., Al-Ahmad, A., Azarin, S. M., Palecek, S. P., & Shusta, E. V. (2014). A
807 retinoic acid-enhanced, multicellular human blood-brain barrier model derived from
808 stem cell sources. *Sci Rep, 4*, 4160. doi:10.1038/srep04160
809 Lippmann, E. S., Azarin, S. M., Kay, J. E., Nessler, R. A., Wilson, H. K., Al-Ahmad, A., . . .
810 Shusta, E. V. (2012). Derivation of blood-brain barrier endothelial cells from human
811 pluripotent stem cells. *Nat Biotechnol, 30*(8), 783-791. doi:10.1038/nbt.2247

812 Martin-Padura, I., Lostaglio, S., Schneemann, M., Williams, L., Romano, M., Fruscella, P., . .
813 . Dejana, E. (1998). Junctional adhesion molecule, a novel member of the
814 immunoglobulin superfamily that distributes at intercellular junctions and modulates
815 monocyte transmigration. *J Cell Biol, 142*(1), 117-127.
816 Morita, K., Sasaki, H., Furuse, M., & Tsukita, S. (1999). Endothelial claudin: claudin-
817 5/TMVCF constitutes tight junction strands in endothelial cells. *J Cell Biol, 147*(1),
818 185-194.
819 Nitta, T., Hata, M., Gotoh, S., Seo, Y., Sasaki, H., Hashimoto, N., . . . Tsukita, S. (2003).
820 Size-selective loosening of the blood-brain barrier in claudin-5-deficient mice. *J Cell*
821 *Biol, 161*(3), 653-660.
822 Ovesny, M., Krizek, P., Borkovec, J., Svindrych, Z., & Hagen, G. M. (2014).
823 ThunderSTORM: a comprehensive ImageJ plug-in for PALM and STORM data
824 analysis and super-resolution imaging. *Bioinformatics, 30*(16), 2389-2390.
825 Reese, T. S., & Karnovsky, M. J. (1967). Fine structural localization of a blood-brain barrier
826 to exogenous peroxidase. *J Cell Biol, 34*(1), 207-217. doi:10.1083/jcb.34.1.207
827 Saunders, N. R., Liddelow, S. A., & Dziegielewska, K. M. (2012). Barrier mechanisms in the
828 developing brain. *Front Pharmacol, 3*, 46. doi:10.3389/fphar.2012.00046
829 Schlingmann, B., Overgaard, C. E., Molina, S. A., Lynn, K. S., Mitchell, L. A., Dorsainvil
830 White, S., . . . Koval, M. (2016). Regulation of claudin/zonula occludens-1 complexes
831 by hetero-claudin interactions. *Nat Commun, 7*, 12276.
832 Sohet, F., Lin, C., Munji, R. N., Lee, S. Y., Ruderisch, N., Soung, A., . . . Daneman, R.
833 (2015). LSR/angulin-1 is a tricellular tight junction protein involved in blood-brain
834 barrier formation. *J Cell Biol, 208*(6), 703-711.
835 Sweeney, M. D., Sagare, A. P., & Zlokovic, B. V. (2018). Blood-brain barrier breakdown in
836 Alzheimer disease and other neurodegenerative disorders. *Nat Rev Neurol, 14*(3), 133-
837 150.
838 van de Linde, S., Loschberger, A., Klein, T., Heidbreder, M., Wolter, S., Heilemann, M., &
839 Sauer, M. (2011). Direct stochastic optical reconstruction microscopy with standard
840 fluorescent probes. *Nat Protoc, 6*(7), 991-1009. doi:10.1038/nprot.2011.336
841 Vanlandewijck, M., He, L., Mae, M. A., Andrae, J., Ando, K., Del Gaudio, F., . . . Betsholtz,
842 C. (2018). A molecular atlas of cell types and zonation in the brain vasculature.
843 *Nature, 554*(7693), 475-480. doi:10.1038/nature25739
844 Vatine, G. D., Al-Ahmad, A., Barriga, B. K., Svendsen, S., Salim, A., Garcia, L., . . .
845 Svendsen, C. N. (2017). Modeling Psychomotor Retardation using iPSCs from
846 MCT8-Deficient Patients Indicates a Prominent Role for the Blood-Brain Barrier. *Cell*
847 *Stem Cell, 20*(6), 831-843.e835. doi:10.1016/j.stem.2017.04.002
848 Vatine, G. D., Barrile, R., Workman, M. J., Sances, S., Barriga, B. K., Rahnama, M., . . .
849 Svendsen, C. N. (2019). Human iPSC-Derived Blood-Brain Barrier Chips Enable
850 Disease Modeling and Personalized Medicine Applications. *Cell Stem Cell, 24*(6),
851 995-1005.e1006. doi:10.1016/j.stem.2019.05.011
852 Zhang, J., Carver, C. M., Choveau, F. S., & Shapiro, M. S. (2016). Clustering and Functional
853 Coupling of Diverse Ion Channels and Signaling Proteins Revealed by Super-
854 resolution STORM Microscopy in Neurons. *Neuron, 92*(2), 461-478.
855 Zhang, Y., Chen, K., Sloan, S. A., Bennett, M. L., Scholze, A. R., O'Keeffe, S., . . . Wu, J. Q.
856 (2014). An RNA-sequencing transcriptome and splicing database of glia, neurons, and
857 vascular cells of the cerebral cortex. *J Neurosci, 34*(36), 11929-11947.
858 Zhao, Z., Nelson, A. R., Betsholtz, C., & Zlokovic, B. V. (2015). Establishment and
859 Dysfunction of the Blood-Brain Barrier. *Cell, 163*(5), 1064-1078.

860 Zhong, Z., Deane, R., Ali, Z., Parisi, M., Shapovalov, Y., O'Banion, M. K., . . . Zlokovic, B.
861 V. (2008). ALS-causing SOD1 mutants generate vascular changes prior to motor
862 neuron degeneration. *Nat Neurosci, 11*(4), 420-422.
863 Zlokovic, B. V. (2008). The blood-brain barrier in health and chronic neurodegenerative
864 disorders. *Neuron, 57*(2), 178-201. doi:10.1016/j.neuron.2008.01.003
865

866

Supplementary Figure S1 Total claudin-5 protein levels in bEND.3 cells and iBMECs TEER are elevated along days in culture

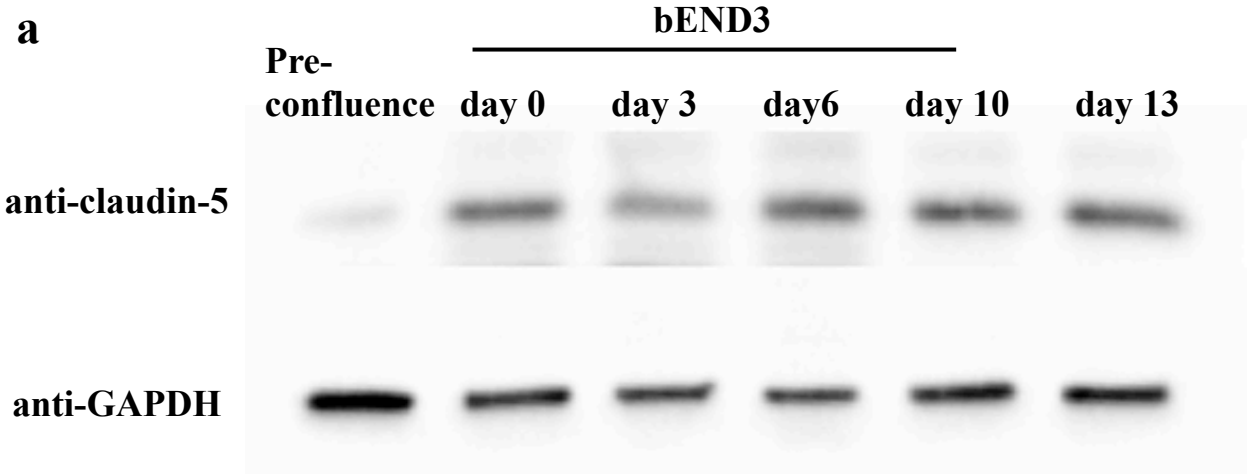

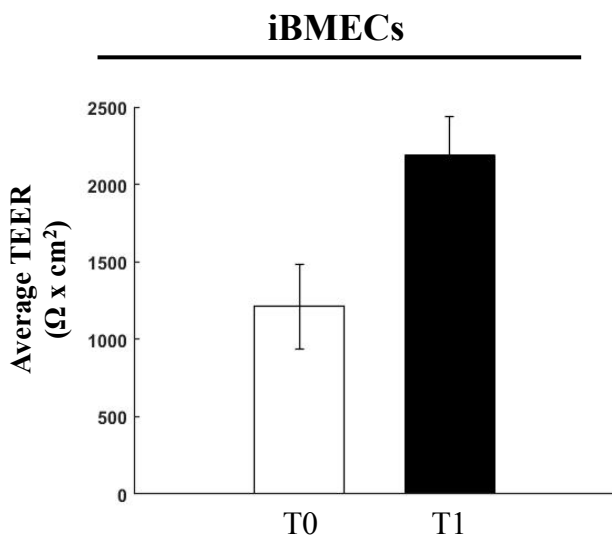

867 **Supplementary Figures**
868

869 **Supplementary Figure S1: Total claudin-5 protein levels in bEND.3 cells and iBMECs**

870 **TEER are elevated with time in culture. a,** Total claudin-5 protein levels in bEND.3 cells

871 rise with time in culture as shown in a representative western blot analysis. n=4. **b,** Enhanced

872 TJ function demonstrated by doubling of TEER (average change in TEER across all

873 experiments) along 2-3 days of human brain microvascular endothelial-like cell (iBMECs)

874 culture (n=4 experiments/12 inserts).

875

Supplementary Figure S2 Claudin-5 clustering properties

a

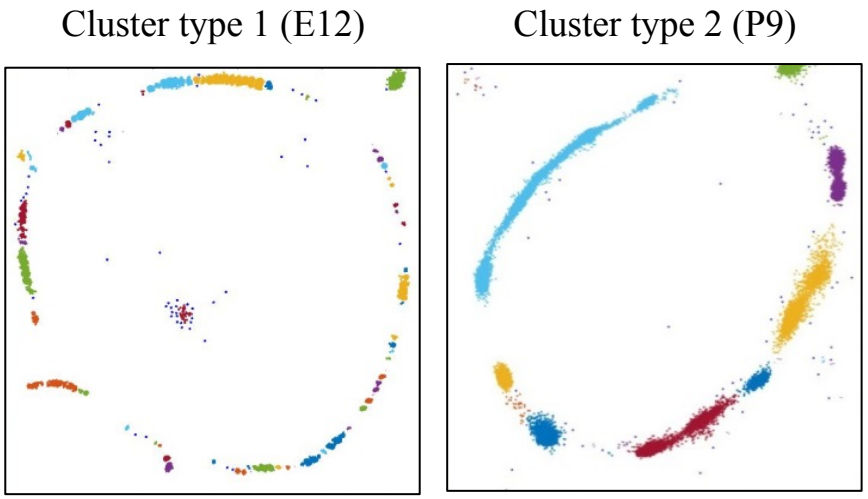

b

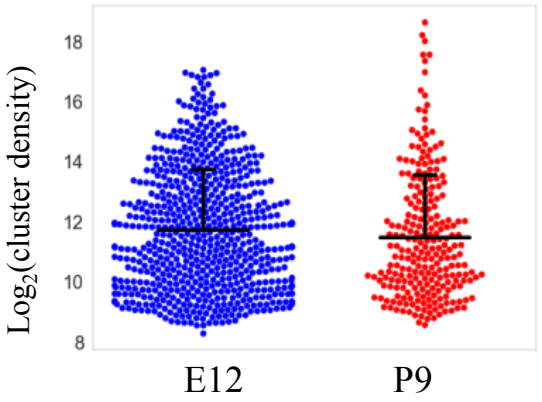

Supplementary Figure S2 Claudin-5 clustering properties. Analysis of Claudin-5 clustering properties along the developmental BBB maturation axis, using custom clustering Matlab code (see methods for details). **a,** dSTORM imaging simulation of claudin-5 immunostaining of E12 and P9 cortical capillary cross-sections (example of the two types of clustering simulations). We assumed that E12 capillaries had a more defused claudin-5 appearance with longer clusters, but further analysis revealed that these are composed of many small clusters with relatively small gaps between them. Signals were defined to be clustered if their 2D location was smaller than 70 nm threshold distance. Cluster pattern visualization showing all points that belong to the same cluster with the same identifying color. **b,** Claudin-5 clustering-properties analysis showed that there were about 2.6 times more discrete clusters per capillary at E12 than at P9 (a set of 20 capillaries of each age). There was no dramatic difference in the distribution of signal densities between the two groups. *n*=3 pups/embryos, 20 capillaries, 657 clusters (E12) and 246 clusters (P9). Data are mean±s.e.m.

Supplementary Figure S3 Molecular organization of ZO1 and occludin in mouse cortical BBB TJs

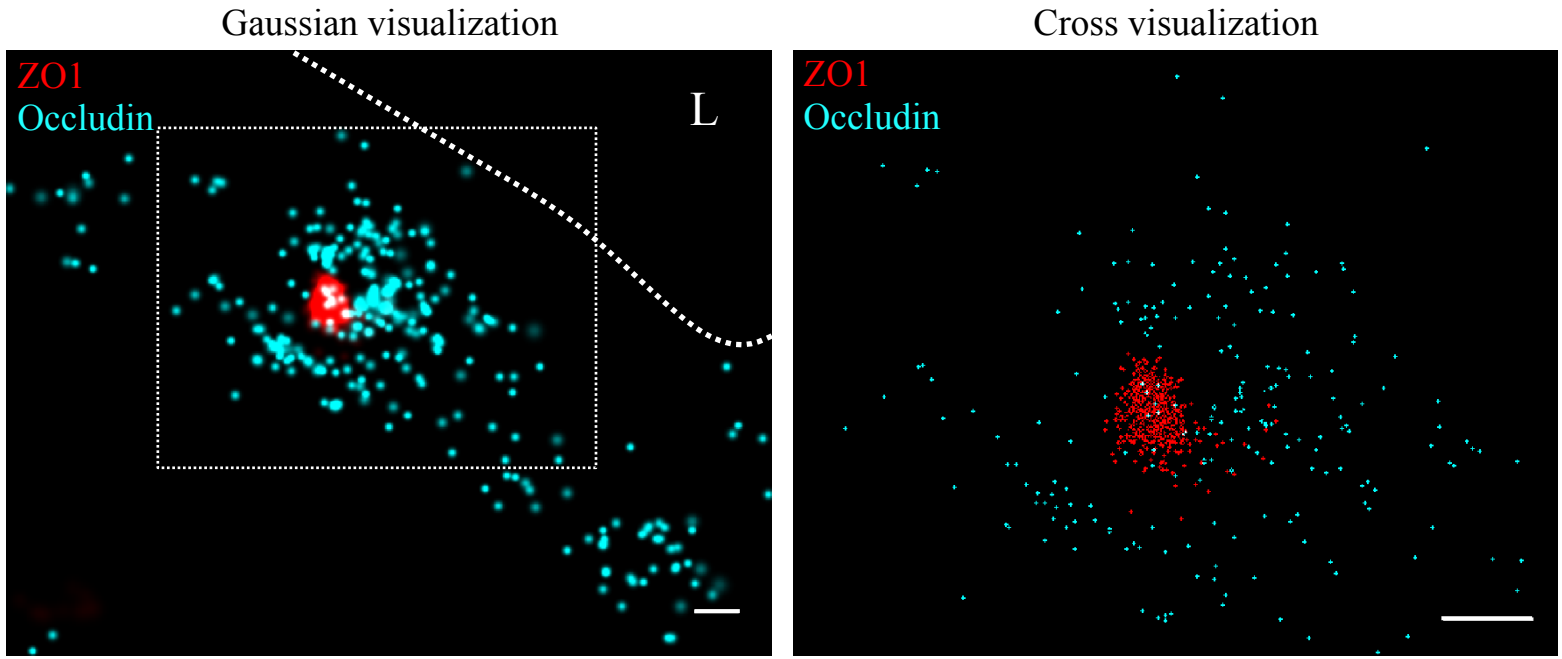

Supplementary Figure S3 Molecular organization of ZO1 and occludin in mouse cortical BBB TJs. Nano-scale molecular organization of TJ proteins in cortical capillaries of wild-type mice (E16). ZO1 display clustered organization (red) whereas occludin (cyan) was much less organized in discrete clusters and had more dispersed organization patterns. 2D-STORM imaging data (left) demonstrates that signals of TJ proteins are in close proximity and sometimes overlap ('Gaussian visualization' in which signal intensity correlates with localization precision). An inset with magnification (right) demonstrates the very high molecular density of ZO1 and the more diffuse organization of occludin ('Cross visualization' shows all resolved signals where each single-molecule signal displays as a cross). Scale bars, 100 nm. *n*=40 capillaries of 4 wild-type pups. L – capillary lumen.

Supplementary Figure S4 Claudin-5 clusters are in close proximity to ER and lysosomal markers

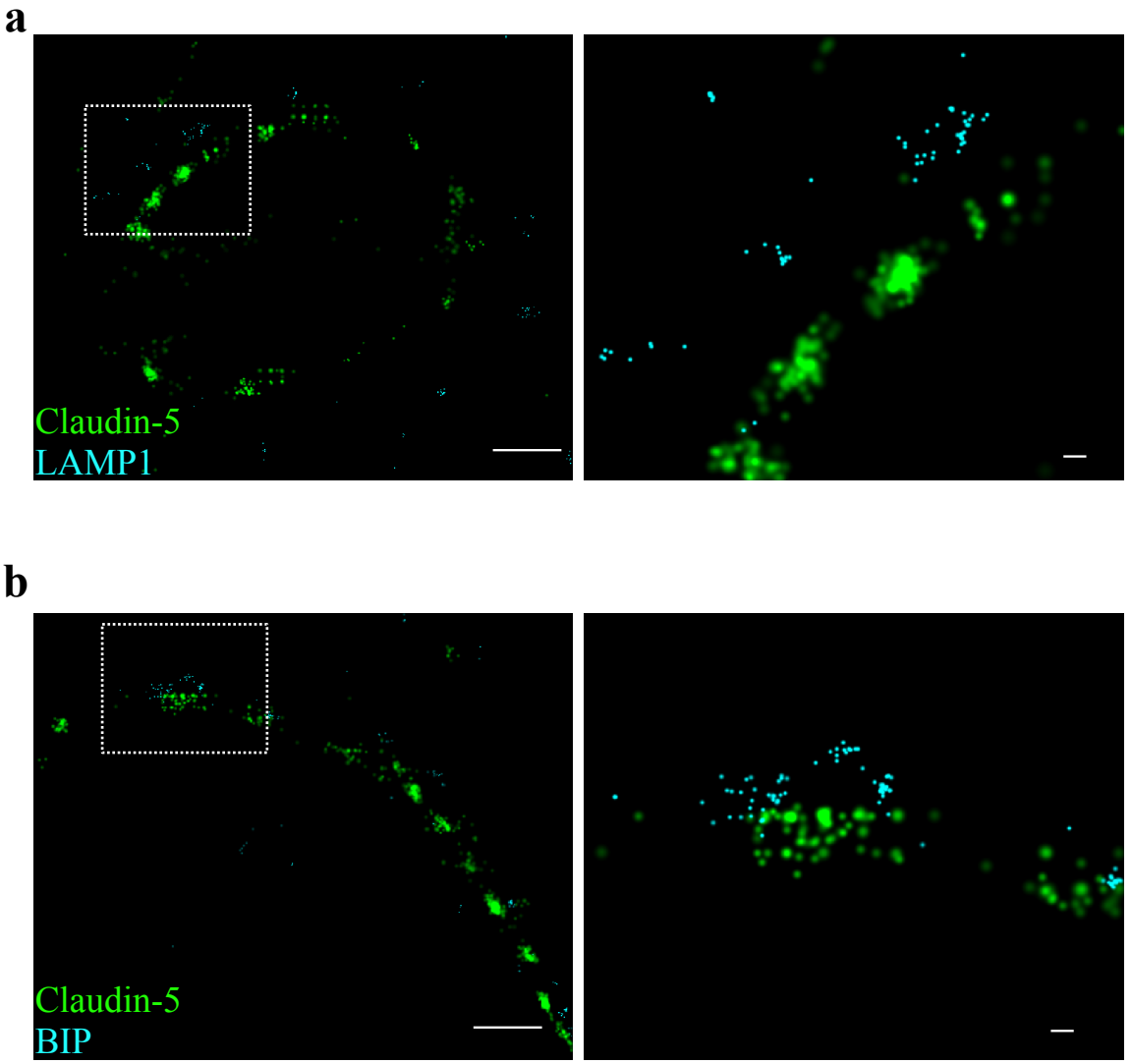

Supplementary Figure S4: Claudin-5 clusters are in close proximity to ER and lysosomal markers. Capillary cross-sections presented multiple claudin-5 clusters, therefore we tested potential claudin-5 localization to different cellular compartments. **a,** Claudin-5 clusters in close proximity with the lysosomal marker LAMP1, suggesting lysosome localization. **b,** Claudin-5 clusters in close proximity with the ER marker BiP, suggesting ER localization. Scale bars, 1 μm and 0.1 μm in insets. n=8 capillaries.

Supplementary Figure S5 clustering analysis – threshold distances

a

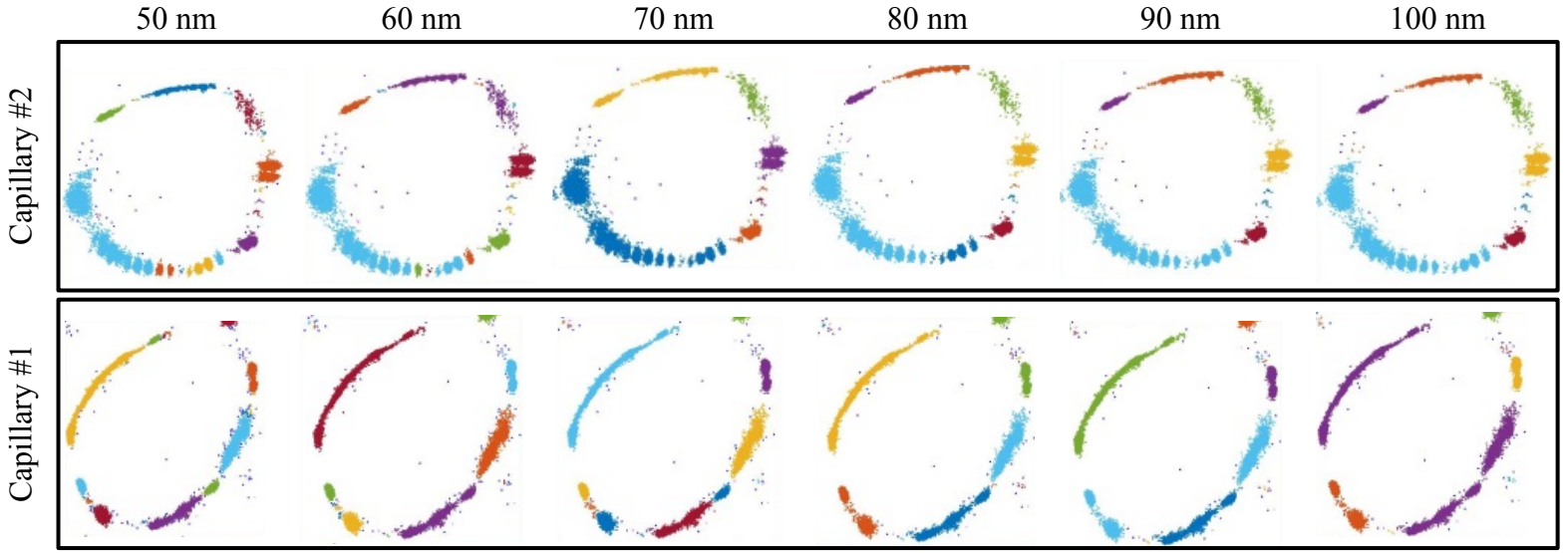

b

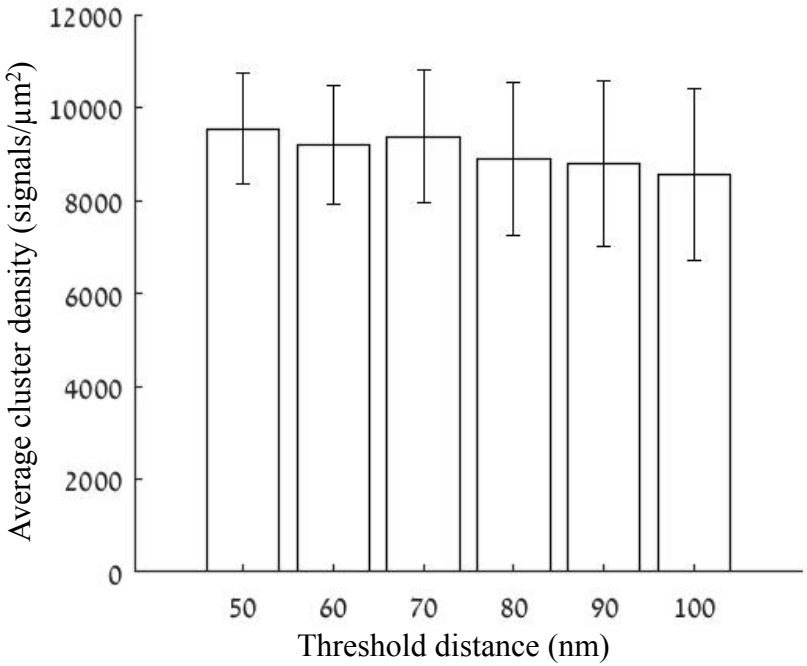

Supplementary Figure S5 Distance threshold used for quantifications of clustering properties. Analysis of claudin-5 clustering properties was done using a custom clustering Matlab code (see methods for details); our code calculated distances between each point and all other points in the point pattern of a Single molecule localization microscopy (SMLM) image. Then, we set a 70 nm distance threshold for defining molecules that belong to the same cluster. This distance threshold used for quantifications was determined based on the following parameters: minimal distance could not be below 40 nm (see methods for antibody labeling strategy); BBB TJs covering continuous contact points, as we evaluated in published TEM imaging data, range approximately up to 100 nm. Finally, we preformed simulation of claudin-5 density in clusters, measured in different threshold distances between 50-100 nm. **a,** Two examples of simulations for claudin-5 cluster densities with different distance thresholds in P9 capillaries. Point patterns are visualized, while showing all points that belong to the same cluster with the same identifying color. Note that while clusters colors might change, the overall cluster organization is similar across tested threshold distances. **b,** Claudin-5 cluster densities quantified using different distance thresholds did not yield significant differences. *n*=8 capillaries. Data are mean±s.e.m.